

**PROVABGS: The Probabilistic Stellar Mass Function of the BGS One-Percent Survey**

CHANGHOON HAHN,<sup>1,\*</sup> JESSICA NICOLE AGUILAR,<sup>2</sup> SHADAB ALAM,<sup>3</sup> STEVEN AHLEN,<sup>4</sup>  
 DAVID BROOKS,<sup>5</sup> SHAUN COLE,<sup>6</sup> AXEL DE LA MACORRA,<sup>7</sup> PETER DOEL,<sup>5</sup>  
 ANDREU A. FONT-RIBERA,<sup>8</sup> JAIME E. FORERO-ROMERO,<sup>9,10</sup> SATYA GONTCHO A GONTCHO,<sup>2</sup>  
 KLAUS HONSCHEID,<sup>11,12</sup> SONG HUANG,<sup>13</sup> THEODORE KISNER,<sup>2</sup> ANTHONY KREMIN,<sup>2</sup>  
 MARTIN LANDRIAU,<sup>2</sup> MARC MANERA,<sup>8</sup> AARON MEISNER,<sup>14</sup> RAMON MIQUEL,<sup>15,8</sup> JOHN MOUSTAKAS,<sup>16</sup>  
 JUNDAN NIE,<sup>17</sup> CLAIRE POPPETT,<sup>2,18,19</sup> GRAZIANO ROSSI,<sup>20</sup> AMÉLIE SAINTONGE,<sup>5</sup>  
 EUSEBIO SANCHEZ,<sup>21</sup> CHRISTOPH SAULDER,<sup>22</sup> MICHAEL SCHUBNELL,<sup>23,24</sup> HEE-JONG SEO,<sup>25</sup>  
 MALGORZATA SIUDEK,<sup>26</sup> FEDERICO SPERANZA,<sup>5</sup> GREGORY TARLÉ,<sup>24</sup> BENJAMIN A. WEAVER,<sup>14</sup>  
 RISA H. WECHSLER,<sup>27,28,29</sup> SIHAN YUAN,<sup>27,29</sup> ZHIMIN ZHOU,<sup>17</sup> AND HU ZOU<sup>17,†</sup>

## ABSTRACT

We present the probabilistic stellar mass function (pSMF) of galaxies in the DESI Bright Galaxy Survey (BGS), observed during the One-Percent Survey. The One-Percent Survey was one of DESI’s survey validation programs conducted from April to May 2021, before the start of the main survey. It used the same target selection and similar observing strategy as the main survey and successfully observed the spectra and redshifts of 143,017 galaxies in the  $r < 19.5$  magnitude-limited BGS Bright sample and 95,499 galaxies in the fainter surface brightness and color selected BGS Faint sample over  $z < 0.6$ . We derive pSMFs from posteriors of stellar mass,  $M_*$ , inferred from DESI photometry and spectroscopy using the Hahn et al. (2022a) PRObabilistic Value-Added BGS (PROVABGS) Bayesian SED modeling framework. We use a hierarchical population inference framework that statistically and rigorously propagates the  $M_*$  uncertainties. Furthermore, we include correction weights that account for the selection effects and incompleteness of the BGS observations. We present the redshift evolution of the pSMF in BGS as well as the pSMFs of star-forming and quiescent galaxies classified using average specific star formation rates from PROVABGS. Overall, the pSMFs show good agreement with previous stellar mass function measurements in the literature. Our pSMFs showcase the potential and statistical power of BGS, which in its main survey will observe  $>100\times$  more galaxies. Moreover, we present the statistical framework for subsequent population statistics measurements using BGS, which will characterize the global galaxy population and scaling relations at low redshifts with unprecedented precision.

*Keywords:* cosmology: observations – galaxies: evolution – galaxies: statistics

\* changhoon.hahn@princeton.edu

† The authors’ affiliations are shown in Appendix D.

## 1. INTRODUCTION

The galaxy population can largely be characterized by a small number of scaling relations (see [Blanton & Moustakas 2009](#), for a review). This empirical network of scaling relations has been established through large galaxy surveys at all wavelengths, with major optical spectroscopic campaigns such as the Sloan Digital Sky Survey (SDSS; [York et al. 2000](#)), Galaxy and Mass Assembly survey (GAMA; [Driver et al. 2011](#)), PRISM Multi-object Survey (PRIMUS; [Coil et al. 2011](#)), and many others playing a crucial role. Population statistics also encode important information, for instance the stellar mass function (SMF) precisely characterizes the overall distribution of the stellar mass ( $M_*$ ) of the galaxy population and its evolution across cosmic history ([Li & White 2009](#); [Marchesini et al. 2009](#); [Moustakas et al. 2013](#); [Muzzin et al. 2013](#); [Leja et al. 2019](#); [Driver et al. 2022](#)).

The relationship between the stellar masses and star formation rates (SFRs) of galaxies reveal a bi-modality in the galaxy population with star-forming galaxies lying on a tightly correlated “star forming sequence” (SFS; [Noeske et al. 2007](#); [Daddi et al. 2007](#); [Salim et al. 2007](#); [Speagle et al. 2014](#); [Hahn et al. 2019](#)). The SFS evolves with redshift, with the SFR of galaxies at fixed mass steadily increasing from  $z = 0$  up to at least  $z \sim 4$ . This is also accompanied by a change in the fraction of quiescent galaxies caused by the quenching of star formation in some galaxies (*e.g.* [Ilbert et al. 2013](#); [Muzzin et al. 2013](#); [Santini et al. 2022](#)). Additional scaling relations invoking quantities such as metallicity (*e.g.* [Tremonti et al. 2004](#); [Mannucci et al. 2010](#)), atomic and molecular gas mass (see reviews in [Tacconi et al. 2020](#); [Saintonge & Catinella 2022](#)), and galaxy size (*e.g.* [Franx et al. 2008](#); [van der Wel et al. 2014](#)) have also been firmly established. These scaling relations and associated population statistics, along with careful measurements of their scatter and redshift evolution, are powerful tools to shed further light on galaxy formation and evolution.

For one, they have the potential to reveal new trends among galaxies undetected by previous observations and open new discovery space. They can also be used to test galaxy formation models spanning empirical models (*e.g.* UNIVERSEMACHINE; [Behroozi et al. 2019](#)), semi-analytic models (*e.g.* [Benson 2012](#); [Henriques et al. 2015](#); [Somerville & Davé 2015](#)), and hydrodynamical simulations (see [Somerville & Davé 2015](#), for a review). Empirical models, for example, have been used to measure the timescale of star formation quenching ([Wetzel et al. 2013](#); [Hahn et al. 2017](#); [Tinker et al. 2017](#)) or the dust content of galaxies ([Hahn et al. 2021](#)).

Furthermore, galaxy observables and their scaling relations can also be used to infer parameters that dictate the physical processes in semi-analytic models (*e.g.* [Henriques et al. 2009](#); [Lu et al. 2014](#); [Henriques et al. 2015](#)). Although full parameter exploration is currently computationally prohibitive for hydrodynamical simulations, they have been extensively compared to observations (*e.g.* [Genel et al. 2014](#); [Davé et al. 2017](#); [Trayford et al. 2017](#); [Dickey et al. 2021](#); [Donnari et al. 2021](#)). Soon, machine learning techniques for accelerating and emulating simulations will enable us to go beyond such comparisons and broadly explore parameter space and galaxy formation models (*e.g.* [Villaescusa-Navarro et al. 2022](#); [Jamieson et al. 2022](#)). While many different approaches are available for expanding our understanding of galaxies, they all require statistically powerful galaxy samples with well-controlled systematics and well-understood selection functions.

One survey that will provide galaxy samples with unprecedented statistical power is the Dark Energy Spectroscopic Instrument (DESI; [Levi et al. 2013](#); [DESI Collaboration et al. 2016a,b](#); [Abareshi et al. 2022](#)). Over its five-year operation, DESI will observe galaxy spectra using the 4-meter Mayall telescope at Kitt Peak National Observatory with a focal plane filled with 5000 robotically actuated fibers that direct the light to ten optical spectrographs ([Schubnell et al. 2016](#); [Silber et al. 2023](#); [Miller et al. 2023](#)). It will observe  $\sim 40$  million galaxy spectra over  $360 < \lambda < 980$  nm with spectral resolution of  $2000 < \lambda/\Delta\lambda < 5500$  over  $\sim 14,000$  deg<sup>2</sup>, a third of the sky. In addition, DESI galaxies will also have photometry from the Legacy Imaging Surveys Data Release 9 (LS; [Dey et al. 2019](#); [Schlegel et al. 2023](#)). The LS is a combination of three public projects (Dark Energy Camera Legacy Survey, Beijing-Arizona Sky Survey ([Zou et al. 2017](#)), and Mayall  $z$ -band Legacy Survey) that jointly imaged the DESI footprint in three optical bands ( $g$ ,  $r$ , and  $z$ ). DESI began observing its main survey on May 14, 2021.

As part of its core observations, DESI is conducting the Bright Galaxy Survey (BGS; [Hahn et al. 2022b](#)). BGS spans the same  $14,000$  deg<sup>2</sup> footprint and will include low redshift  $z < 0.6$  galaxies that can be observed during bright time, when the night sky is  $\sim 2.5\times$  brighter than nominal dark conditions. BGS will provide two galaxy samples: the BGS Bright sample, a  $r < 19.5$  magnitude-limited sample of  $\sim 10$  million galaxies, and the BGS Faint sample, a fainter  $19.5 < r < 20.175$  sample of  $\sim 5$  million galaxies selected using a surface brightness and color. The selection and completeness of the BGS samples are characterized in detail in [Hahn et al. \(2022b\)](#) (see also [Myers et al. 2023](#)). Compared to the seminal SDSS main galaxy survey, BGS will provide a galaxy sample two magnitudes deeper, over twice the sky, and double the median redshift  $z \sim 0.2$ . It will observe a broader range of galaxies than previous surveys and provide an opportunity to measure galaxy population statistics with unprecedented precision.

BGS will also be accompanied by a value-added catalog: the Probabilistic Value-Added BGS (PROVABGS; [Hahn et al. 2022a](#); [Kwon et al. 2022](#)). For every BGS galaxy, PROVABGS will provide physical properties including stellar mass ( $M_*$ ), average star formation rate ( $\overline{\text{SFR}}$ ), stellar metallicity ( $Z_*$ ), stellar age ( $t_{\text{age}}$ ), and dust content. These galaxy properties will be derived from state-of-the-art Spectral Energy Distribution (SED) modeling of both DESI photometry and spectroscopy in a full Bayesian inference framework. The SED model is designed to minimize model mis-specification by using highly flexible non-parametric star formation and metallicity histories as well as a flexible dust attenuation model. Furthermore, the properties will be inferred using a fully Bayesian inference framework and will thus provide statistically rigorous estimates of uncertainties and degeneracies among the properties. Ultimately, PROVABGS will provide consistently measured galaxy properties that will enable analyses to take full advantage of the statistical power of BGS with new techniques and approaches.

A key application for PROVABGS will be measuring population statistics using a statistically rigorous methodology that correctly propagates the uncertainties in galaxy property measurements. Current population statistics are by and large derived from simply binning best-fit point estimates of galaxy properties. [Malz & Hogg \(2020\)](#) demonstrated, in the context of inferring redshift distributions from individual photometric redshift measurements, that using point estimates is statistically

incorrect and can lead to biased redshift distributions. Similarly, the point estimate approach can also lead to biased population statistics.

Instead, we can estimate population statistics from combining individual PROVABGS posteriors of galaxy properties using population inference in a hierarchical Bayesian framework (*e.g.* Hogg et al. 2010; Foreman-Mackey et al. 2014; Baronchelli et al. 2020). This approach correctly propagates the uncertainties in the galaxy properties from the individual posteriors of galaxies. As a result, they significantly improve the accuracy of population statistics measurements and will enable more accurate measurements of key galaxy scaling relations. In this work, we present the first such population statistics measurement for BGS: the probabilistic stellar mass function (pSMF).

In particular, we present the pSMF of BGS galaxies observed during the DESI One-Percent Survey, a survey validation program conducted before the main survey operations. We also present the statistical methodology for the population inference as well as our methods for accounting for observational systematics and incompleteness. We begin in Section 2 with an overview of the BGS galaxies observed during the DESI One-Percent Survey. Then, in Section 3, we briefly summarize the PROVABGS SED modeling framework used to infer the physical properties of the BGS galaxies. Afterward, we present the pSMF inferred from the BGS observations in Section 4. We summarize and discuss our results in Section 5. Throughout this work, we assume AB magnitudes and a flat  $\Lambda$ CDM cosmology described by the final Planck results (Planck Collaboration et al. 2014):  $\Omega_m = 0.307$ ,  $\Omega_b = 0.0483$ ,  $H_0 = 67.8 \text{ km s}^{-1} \text{ Mpc}^{-1}$ ,  $A_s = 2.19 \times 10^{-9}$ ,  $n_s = 0.9635$ .

## 2. THE DESI BRIGHT GALAXY SURVEY: ONE-PERCENT SURVEY

DESI began its five years of operations in May 14, 2021 (Schlafly et al. 2023; Kirkby et al. 2023). Before its start, DESI conducted the Survey Validation (SV) campaign to verify that the survey will meet its scientific and performance requirements. The SV campaign was divided into two main programs: the first, SV1, characterized the survey’s performance for different observing conditions and was used to optimize sample selection. The second, the One-Percent Survey (or SV3), observed a dataset that can be used for representative clustering measurements and deliver a ‘truth’ sample with high completeness over an area at least 1% of the expected main survey footprint. We refer readers to DESI Collaboration et al. (2023a) and DESI Collaboration et al. (2023b) for details on the DESI SV programs. For details on how DESI targets are selected, we refer readers to Cooper et al. (2022); Zhou et al. (2023); Raichoor et al. (2023), and Chaussidon et al. (2023)<sup>1</sup>. In this work, we focus on BGS galaxies observed during the One-Percent Survey.

The One-Percent Survey was observed on 38 nights from April 2021 to the end of May 2021. During this time, DESI observed 288 bright time exposures that cover 214 BGS ‘tiles’, planned DESI pointings. The tiles were arranged so that a set of 11 overlapping tiles has their centers arranged around a 0.12 deg circle, forming a ‘rosette’ completeness pattern. In total, the One-Percent Survey observed 20 rosettes covering  $180 \text{ deg}^2$  spanning the northern galactic cap (see Figure 1 in Hahn et al. 2022b).

<sup>1</sup> See also Allende Prieto et al. (2020); Raichoor et al. (2020); Ruiz-Macias et al. (2020); Yèche et al. (2020); Zhou et al. (2020) for details on preliminary target selection and Lan et al. (2023); Alexander et al. (2023) for the visual inspection of spectra used to inform target selection.

All BGS spectra observed during the One-Percent Survey are reduced using the ‘fuji’ version of the DESI spectroscopic data reduction pipeline (Guy et al. 2023). First, spectra are extracted from the spectrograph CCDs using the *spectroperfectionism* algorithm of Bolton & Schlegel (2010). Then, fiber-to-fiber variations are corrected by flat-fielding and a sky model, empirically derived from sky fibers, is subtracted from each spectrum. Afterwards, the fluxes in the spectra are calibrated using stellar model fits to standard stars. The final processed spectra is then derived by co-adding the calibrated spectra across exposures of the same tile. In total, DESI observed spectra of 155,022 BGS Bright and 109,418 BGS Faint targets during the One-Percent Survey.

For each spectrum, redshift is measured using *Redrock*<sup>2</sup> (Bailey et al. 2023; Brodzeller et al. 2023), a redshift fitting algorithm that uses  $\chi^2$  minimization computed from a linear combination of Principal Component Analysis (PCA) basis spectral templates in three template classes (“stellar”, “galaxy”, and “quasar”). *Redrock* also provides measures of redshift uncertainty, ZERR and redshift confidence,  $\Delta\chi^2$ , which corresponds to the difference between the  $\chi^2$  values of the best-fit model and the next best-fit model. We restrict our sample to galaxy targets with reliable redshift measurements, as defined in Hahn et al. (2022b) and DESI Collaboration et al. (2023a): we only keep targets with spectra classified as galaxy spectra by *Redrock*, no *Redrock* warning flags,  $\Delta\chi^2 > 40$ , and *Redrock* redshift uncertainty ZERR  $< 0.0005(1+z)$ . We also exclude any targets observed using malfunctioning fiber positioners. Lastly, we impose a redshift range of  $0 < z < 0.6$ . After these cuts, our One-Percent Survey BGS sample includes 143,074 BGS Bright galaxies and 96,771 BGS Faint galaxies.

### 3. PROVABGS SED MODELING

For each BGS galaxy, we derive its  $M_*$  and other physical properties, such as  $\overline{\text{SFR}}$ , mass-weighted metallicity ( $Z_{\text{MW}}$ ), and mass-weighted stellar age ( $t_{\text{age,MW}}$ ), from DESI photometry and spectroscopy using the PROVABGS SED modeling framework (Hahn et al. 2022a). PROVABGS models galaxy SEDs using stellar population synthesis with a non-parametric star-formation history (SFH) with a starburst, a non-parametric metallicity history (ZH) that evolves with time, and a flexible dust attenuation prescription. The non-parameteric SFH and ZH prescriptions are derived from SFHs and ZHs of simulated galaxies in the Illustris hydrodynamic simulation (Vogelsberger et al. 2014; Genel et al. 2014; Nelson et al. 2015) and provide compact and flexible representations of SFHs and ZHs. For the stellar population synthesis, PROVABGS uses the Flexible Stellar Population Synthesis (FSPS; Conroy et al. 2009, 2010) model with MIST isochrones (Paxton et al. 2011, 2013, 2015; Choi et al. 2016; Dotter 2016), Chabrier (2003) initial mass function (IMF), and a combination of MILES (Sánchez-Blázquez et al. 2006) and BaSeL (Lejeune et al. 1997, 1998; Westera et al. 2002) spectral libraries. The PROVABGS SED model excludes emission lines by masking the wavelength ranges of emission lines. For dust, PROVABGS uses the two component Charlot & Fall (2000) attenuation model with birth cloud and diffuse dust components and does not include re-radiated dust emission.

Furthermore, PROVABGS provides a Bayesian inference framework that infers full posterior probability distributions of the SED model parameter:  $p(\theta | \mathbf{X}^{\text{photo}}, \mathbf{X}^{\text{spec}})$ , where  $\mathbf{X}^{\text{photo}}$  represents the

<sup>2</sup> <https://redrock.readthedocs.io>

photometry and  $\mathbf{X}^{\text{spec}}$  represents the spectroscopy. In total,  $\theta$  has 13 parameters:  $M_*$ , 6 parameters specifying the SFH ( $\beta_1, \beta_2, \beta_3, \beta_4, f_{\text{burst}}, t_{\text{burst}}$ ), 2 parameters specifying ZH ( $\gamma_1, \gamma_2$ ), 3 parameters specifying dust attenuation ( $\tau_{\text{BC}}, \tau_{\text{ISM}}, n_{\text{dust}}$ ), and a nuisance parameter for the fiber aperture effect. Posteriors accurately estimate uncertainties and degeneracies among galaxy properties. Furthermore, they are essential for rigorous hierarchical population inference as we later demonstrate.

In practice, accurately estimating a 13-dimensional posterior requires a large number ( $\gtrsim 100,000$ ) of SED model evaluations, which requires prohibitive computational resources — roughly 10 CPU hours per galaxy. To address this challenge, PROVABGS samples the posterior using the Karamanis & Beutler (2020) ensemble slice Markov Chain Monte Carlo (MCMC) sampling with the ZEUS Python package<sup>3</sup>. PROVABGS further accelerates the inference by using neural emulators for the SED models. The emulators are accurate to subpercent level and  $> 100\times$  faster than the original SED model based on FSPS (Kwon et al. 2022). With ZEUS and neural emulation, deriving a posterior takes  $\sim 5$  min per galaxy with PROVABGS. Moreover, Hahn et al. (2022a) used forward-modeled synthetic BGS observations to demonstrate PROVABGS can accurately infer  $M_*$  over the full expected  $M_*$  range of BGS.

In Figure 1, we demonstrate the PROVABGS SED modeling framework for a randomly selected BGS Bright galaxy with  $z = 0.2768$  (target ID: 39627769595825146). In the top panels, we present the posteriors of galaxy properties,  $M_*$ ,  $\overline{\text{SFR}}$ ,  $Z_{\text{MW}}$ , and  $t_{\text{age,MW}}$ , inferred from DESI photometry and spectroscopy. We mark the 12, 40, 68, and 86 percentiles of the posterior with the contours. The posteriors illustrate that we can precisely measure the properties of BGS galaxies from DESI photometry and spectroscopy. Furthermore, with the full posterior, we accurately estimate the uncertainties on the galaxy properties and the degeneracies among them (*e.g.*  $M_*$  and  $\overline{\text{SFR}}$ ). In the bottom panels, we compare the PROVABGS SED model prediction using the best-fit parameter values (black) to DESI observations (blue). The bottom left panel compares the optical  $g$ ,  $r$ , and  $z$ -band photometry while the right panel compares the spectra. For reference, we also include the observed spectra with coarser wavelength binning (azure). The comparison shows good agreement between the best-fit model and the observations.

We derive a PROVABGS posterior (*e.g.* Figure 1) for every galaxy in the DESI One-Percent Survey. In Figure 2, we present the best-fit  $M_*$  measurements as a function of  $z$  for the BGS galaxies in the DESI One-Percent Survey. We mark the galaxies in the BGS Bright sample in blue and the ones in the BGS Faint sample in orange.

#### 4. RESULTS

From the posteriors of galaxy properties inferred using PROVABGS (Section 3), we derive the marginalized 1D posterior of  $M_*$ ,  $p(M_* | \mathbf{X}_i)$ , from observed spectrophotometry  $\mathbf{X}_i$  of galaxy  $i$ . Using these posteriors, we can estimate the probabilistic SMF (pSMF) of BGS galaxies using population inference in a hierarchical Bayesian framework (*e.g.* Hogg et al. 2010; Foreman-Mackey et al. 2014; Baronchelli et al. 2020). In other words, we can infer  $p(\phi | \{\mathbf{X}_i\})$ , the probability distribution of  $\phi$  given the BGS observations,  $\{\mathbf{X}_i\}$ .  $\phi$  is the set of population hyperparameters that describe the

<sup>3</sup> <https://zeus-mcmc.readthedocs.io/>

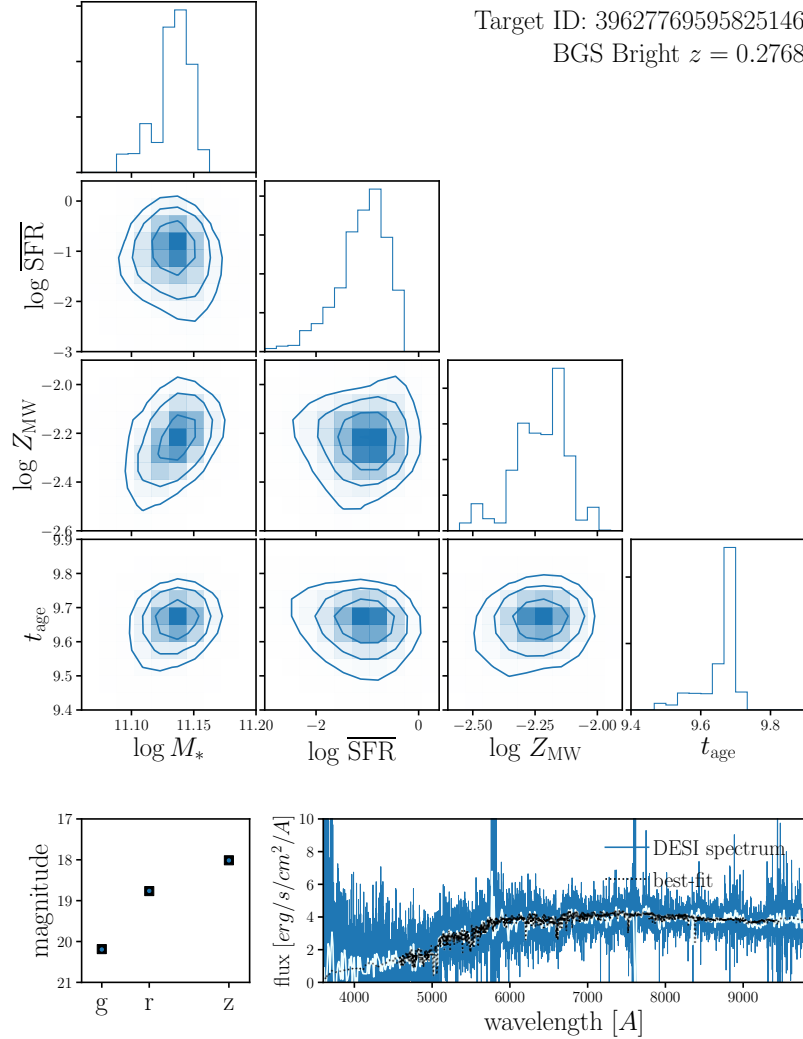


**Figure 1.** *Top panels:* Posteriors of galaxy properties,  $M_*$ ,  $\overline{\text{SFR}}$ ,  $Z_{\text{MW}}$ , and  $t_{\text{age,MW}}$ , for a randomly selected BGS Bright galaxy with  $z = 0.2768$  (target ID: 39627769595825146) inferred using the PROVABGS SED modeling framework from DESI photometry and spectroscopy. The contours mark the 12, 40, 68, and 86 percentiles of the posterior. With the PROVABGS posteriors, we accurately estimate the galaxy properties, their uncertainties, and any degeneracies among them. *Bottom panels:* Comparison of the best-fit PROVABGS SED model prediction (black) to observations (blue). We compare the  $g$ ,  $r$ , and  $z$ -band photometry in the left panel and spectra in the right panel. We include the observed spectra with coarser binning for clarity (azure). We use PROVABGS to infer the posterior of galaxy properties for every BGS galaxy in the DESI One-Percent Survey.

pSMF,  $\Phi(M_*; \phi)$ . This approach is statistically rigorous and enables us to correctly propagate the uncertainties in our  $M_*$  measurements to the pSMF.

In this work, we estimate the pSMF using a Gaussian Mixture Model (GMM; Press et al. 1992; McLachlan & Peel 2000; Blanton et al. 2003), which provides a highly flexible description of the  $M_*$

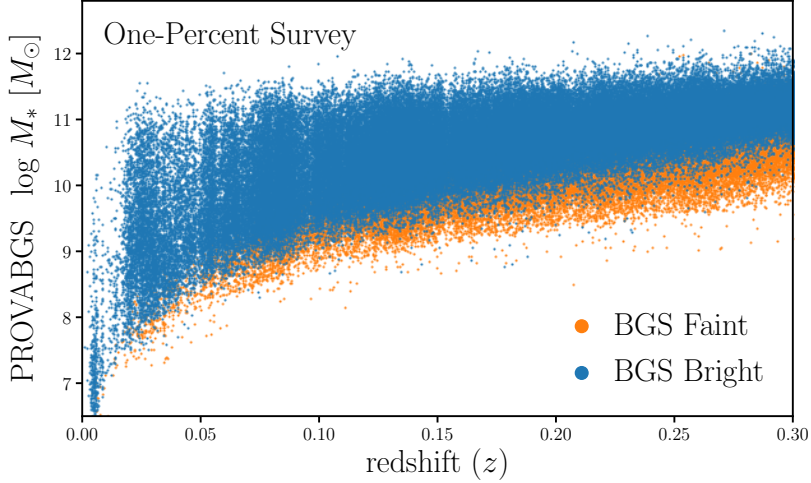


**Figure 2.**  $M_*$  as a function of  $z$  of BGS Bright (blue) and Faint (orange) galaxies in the DESI One-Percent Survey. For  $M_*$ , we use the best-fit values derived using PROVABGS. BGS Bright is a magnitude-limited sample to  $r < 19.5$  while BGS Faint includes fainter galaxies  $19.5 < r < 20.175$  selected using surface brightness ( $r_{\text{fiber}}$ ) and color (Hahn et al. 2022b). In total, we infer the posteriors of 143,017 BGS Bright and 95,499 BGS Faint galaxies across  $z < 0.6$  in the DESI One-Percent Survey.

distribution:

$$\Phi(M_*; \phi) = \sum_{j=1}^k \mathcal{N}(M_*; \phi_j). \quad (1)$$

$k$  is the number of Gaussian components and  $\phi_j$  is the mean and standard deviation of the  $j^{\text{th}}$  Gaussian component of the GMM. Previous works have used parametric functions (*e.g.* the Schechter function) to describe the pSMF (*e.g.* Leja et al. 2019). We opt for GMMs in order to produce a non-parametric measurement of the pSMF. In a subsequent work, Speranza et al. (in prep.), we will present the BGS pSMF measured using a parametric model with continuous redshift evolution.

To infer  $p(\phi | \{\mathbf{X}_i\})$ , we follow the same approach described in Hahn et al. (2022a):

$$p(\phi | \{\mathbf{X}_i\}) = \frac{p(\phi) p(\{\mathbf{X}_i\} | \phi)}{p(\{\mathbf{X}_i\})} \quad (2)$$

$$= \frac{p(\phi)}{p(\{\mathbf{X}_i\})} \int p(\{\mathbf{X}_i\} | \{\theta_i\}) p(\{\theta_i\} | \phi) d\{\theta_i\}. \quad (3)$$

$$= \frac{p(\phi)}{p(\{\mathbf{X}_i\})} \prod_{i=1}^N \int p(\mathbf{X}_i | \theta_i) p(\theta_i | \phi) d\theta_i \quad (4)$$

$$= \frac{p(\phi)}{p(\{\mathbf{X}_i\})} \prod_{i=1}^N \int \frac{p(\theta_i | \mathbf{X}_i) p(\mathbf{X}_i)}{p(\theta_i)} p(\theta_i | \phi) d\theta_i \quad (5)$$

$$= p(\phi) \prod_{i=1}^N \int \frac{p(\theta_i | \mathbf{X}_i) p(\theta_i | \phi)}{p(\theta_i)} d\theta_i. \quad (6)$$

We can estimate the integral using  $S_i$  Monte Carlo samples from the individual posteriors  $p(\theta_i | \mathbf{X}_i)$ :

$$p(\phi | \{\mathbf{X}_i\}) \approx p(\phi) \prod_{i=1}^N \frac{1}{S_i} \sum_{j=1}^{S_i} \frac{p(\theta_{i,j} | \phi)}{p(\theta_{i,j})}. \quad (7)$$

$p(\phi)$  and  $p(\theta_{i,j})$  are the priors on the population hyperparameters and the SED model parameters. We use uniform distributions,  $p(\phi) = 1$  and  $p(\theta_{i,j}) = 1$ , for both priors in this work.

Since the sample of BGS galaxies is not volume limited and complete as a function of  $M_*$ , we must account for selection effects and incompleteness when estimating the pSMF. Thus, we include weights derived from  $z_i^{\max}$ , the maximum redshift that galaxy  $i$  could have and still be included in the BGS samples. We derive  $z_i^{\max}$  for each galaxy by redshifting the SED predicted by the best-fit (maximum likelihood) parameters and determining the maximum  $z$  that the galaxy could be placed before it falls out of the survey selection. We use the best-fit parameters, rather than, *e.g.*, samples drawn from the posteriors. However, this does not have a significant effect because BGS spans a relatively narrow redshift range and BGS galaxies are primarily selected using  $r$ -band magnitudes. The  $r$ -band bandpass lies at the center of DESI spectral wavelength range so the SED models used to calculate  $z_{\max}$  would be well constrained by the observed spectrum. We then derive the comoving volume,  $V_i^{\max}$ , out to  $z_i^{\max}$ , and include a factor of  $1/V_i^{\max}$  in the galaxy weight  $w_i$ .

Next, we include correction weights for spectroscopic incompleteness driven by fiber assignment and redshift failures. The incompleteness from fiber assignment is due to the fact that DESI is not able to assign fibers to all galaxies included in the BGS target selection. Furthermore, there is significant variation in the assignment probability due to the clustering of galaxies. Meanwhile, incompleteness from redshift failure is caused by the fact that we do not successfully measure the redshift for every spectrum. The redshift failure rate depends significantly on the surface brightnesses of the galaxies and the signal-to-noise ratio of the spectra. We describe how we derive the incompleteness correction weights for fiber assignment and redshift failures,  $w_{i,\text{FA}}$  and  $w_{i,\text{ZF}}$ , in Appendix A. Each BGS galaxy is assigned a weight of  $w_i = (w_{i,\text{FA}} \times w_{i,\text{ZF}})/V_i^{\max}$ .

We modify Eq. 4 to include galaxy weights,  $w_i$ :

$$p(\phi | \{\mathbf{X}_i\}) \approx \frac{p(\phi)}{\prod_{i=1}^N p(\mathbf{X}_i)^{w_i}} \prod_{i=1}^N \left( \int p(\mathbf{X}_i | \theta_i) p(\theta_i | \phi) d\theta_i \right)^{w_i} \quad (8)$$

$$\approx \frac{p(\phi)}{\prod_{i=1}^N p(\mathbf{X}_i)^{w_i}} \prod_{i=1}^N \left( \sum_{j=1}^{S_i} \frac{p(\theta_{i,j} | \phi)}{p(\theta_{i,j})} \right)^{w_i} \quad (9)$$

$$\approx \frac{p(\phi)}{\prod_{i=1}^N p(\mathbf{X}_i)^{w_i}} \prod_{i=1}^N \left( \sum_{j=1}^{S_i} \frac{\Phi(\theta_{i,j}; \phi)}{p(\theta_{i,j})} \right)^{w_i}. \quad (10)$$

The weights are included in the exponent so, for example, a galaxy with  $w_i = 2$  would have the same contribution to  $p(\phi | \{\mathbf{X}_i\})$  as two galaxies with  $w_i = 1$ .

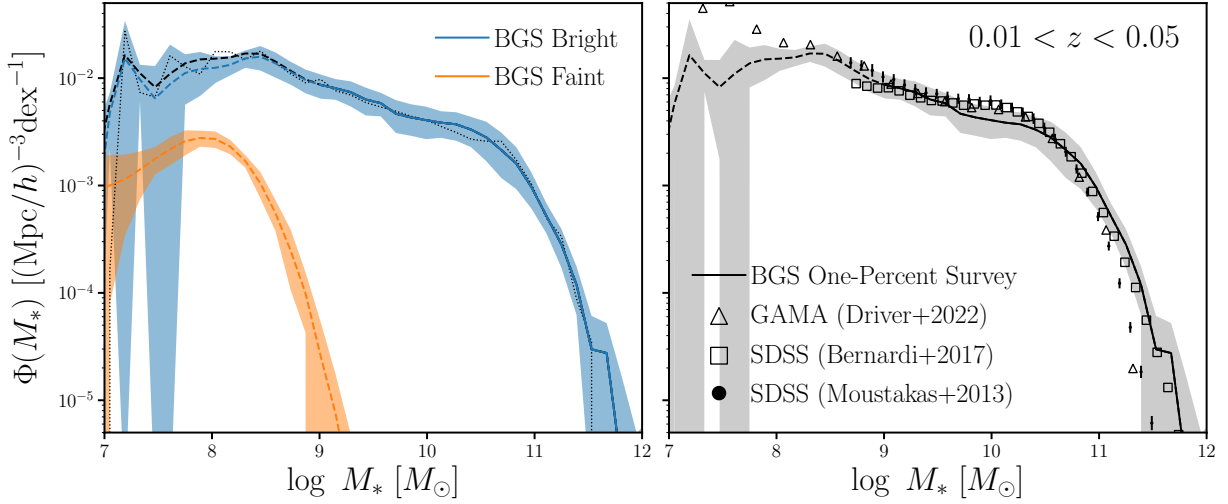


**Figure 3.** The probabilistic SMF (pSMF) of BGS galaxies in the One-Percent Survey at  $0.01 < z < 0.05$  (black line). In the left panel, we present the pSMFs of BGS Bright (blue) and Faint (orange) galaxies, separately. We also include the SMF measured using the standard point estimate approach (black dotted), which underestimates the SMF at the low and high mass ends. We represent uncertainties on the pSMF, estimated using a standard jackknife technique (Appendix B), in the shaded regions. The solid line represents the pSMF above the completeness limit  $M_* > M_{\text{lim}} = 10^{8.975} M_\odot$  (Appendix C). In the right panel, we include SMF measurements from previous spectroscopic surveys for comparison: SDSS (Moustakas et al. 2013; Bernardi et al. 2017) and GAMA (Driver et al. 2022). Overall, the pSMF of BGS are in good agreement with SMF measurements from previous surveys.

In practice, we do not derive the full posterior  $p(\phi | \{\mathbf{X}_i\})$ . Instead we derive the maximum a posteriori (MAP) hyperparameter  $\phi_{\text{MAP}}$  that maximizes  $p(\phi | \{\mathbf{X}_i\})$  or  $\log p(\phi | \{\mathbf{X}_i\})$ . We expand,

$$\log p(\phi | \{\mathbf{X}_i\}) \approx \log p(\phi) + \sum_{i=1}^N w_i \log \left( \sum_{j=1}^{S_i} \frac{\Phi(\theta_{i,j}; \phi)}{p(\theta_{i,j})} \right). \quad (11)$$

Since the first two terms are constant, we derive  $\phi_{\text{MAP}}$  by maximizing

$$\max_{\phi} \sum_{i=1}^N w_i \log \left( \sum_{j=1}^{S_i} \frac{\Phi(\theta_{i,j}; \phi)}{p(\theta_{i,j})} \right), \quad (12)$$

using the ADAM optimizer (Kingma & Ba 2017). We derive  $\phi_{\text{MAP}}$  for BGS galaxies in redshift bins of width  $\Delta z = 0.04$ , starting from  $z = 0.01$ , in order to examine the redshift evolution of the SMF within BGS.

#### 4.1. The Probabilistic Stellar Mass Function

We present the pSMF of BGS galaxies in the One-Percent Survey in Figure 3 (black line) at  $0.01 < z < 0.05$ . In the left panel, we also present the pSMFs of the BGS Bright (blue) and Faint (orange) galaxies, separately. BGS Bright galaxies are selected using a  $r < 19.5$  magnitude limit. As a result, the BGS Bright sample is  $M_*$  complete above  $M_{\text{lim}} > 10^{8.975} M_\odot$ . We derive  $M_{\text{lim}}$  in Appendix C

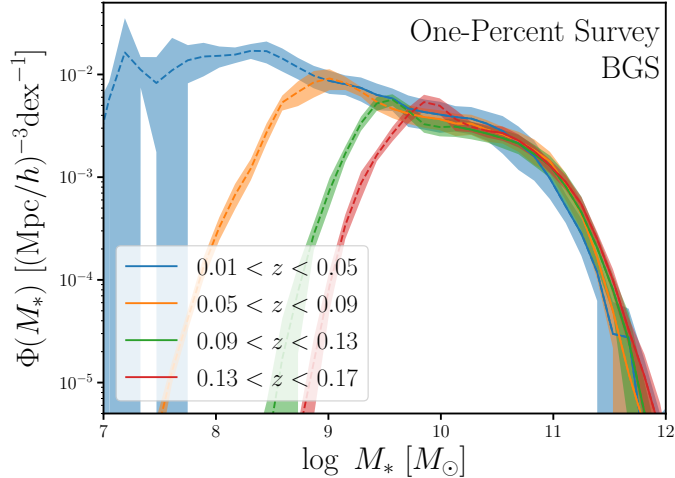


**Figure 4.** The BGS pSMF over the redshift range  $0.01 < z < 0.17$  in bins of  $\Delta z = 0.04$ . The shaded regions represent the uncertainties on the pSMF, estimated using a standard jackknife technique. The solid lines represent the pSMF above the completeness limit  $M_* > M_{\text{lim}}$  while the dashed lines represent the pSMF below the limit. We find no significant redshift evolution of the pSMFs over this range. The main BGS survey will observe  $> 100\times$  more galaxies than the One-Percent Survey and will characterize the pSMF redshift evolution even more precisely.

and mark the pSMF above the completeness limit in solid and below the limit in dashed. Meanwhile, the BGS Faint sample is selected using a surface brightness and color selection. It includes fainter galaxies,  $19.5 < r < 20.175$ , with overall lower  $M_*$  than BGS Bright. The shaded regions represent the uncertainties of the pSMF, which we derive using a standard jackknife technique (Appendix B). The jackknife uncertainties conservatively estimate the combined uncertainties from the population inference as well as cosmic variance (Norberg et al. 2009).

We also include the SMF estimated using the standard point estimate approach (black dotted), derived using the maximum likelihood  $M_*$  point estimates with the same galaxy weights,  $w_i$ . At intermediate  $M_*$  range,  $10^9 < M_* < 10^{11} M_\odot$ , we find good agreement with the pSMF. However, the standard approach significantly underestimates the SMF outside this  $M_*$  range. These discrepancies are due to the fact that point estimates of  $M_*$  ignore the uncertainties in the inferred  $M_*$ . The impact is significant at the most massive end of the SMF with fewer galaxies. It is also significant at the least massive end where the observations have lower signal-to-noise so the individual  $M_*$  posteriors are broader. The discrepancies are present in all other redshift bins and underscore the importance of correctly propagating the  $M_*$  uncertainties.

In the right panel, we compare the BGS pSMF to SMF measurements from previous spectroscopic surveys: SDSS (black circle and square; Moustakas et al. 2013; Bernardi et al. 2017) and GAMA (black triangle Driver et al. 2022). We note that there is significant variance in SMF measurements in the literature, especially at the high  $M_*$  end. This is partly due to the different modeling methodologies used to derive  $M_*$ , which can contribute  $>0.1$  dex discrepancies (Pacifi et al. 2023). Furthermore, there are also discrepancies due to photometric corrections applied to SDSS photometry, assumptions

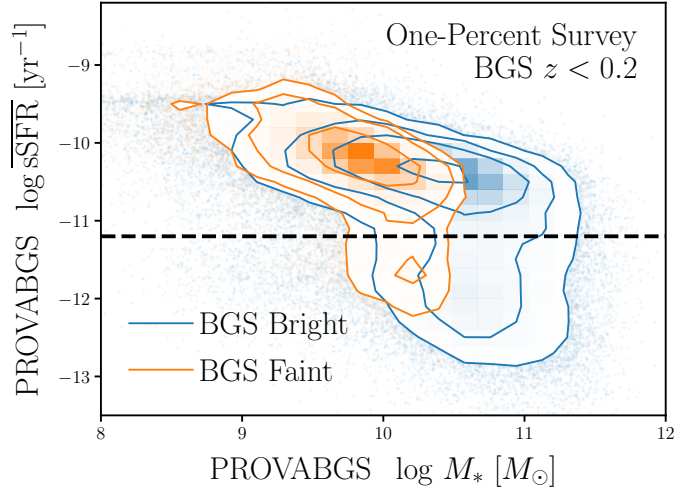


**Figure 5.** The  $M_* - \overline{\text{sSFR}}$  distribution of BGS galaxies at  $z < 0.2$ .  $\overline{\text{sSFR}}$  is derived using  $\overline{\text{SFR}}$ , average SFR over the last 1 Gyr, inferred using PROVABGS. The  $M_* - \overline{\text{sSFR}}$  distribution is bimodal with star-forming galaxies lying on the star-forming sequence. We classify galaxies with  $\overline{\text{sSFR}} > 10^{-11.2} \text{ yr}^{-1}$  as star-forming galaxies and  $\overline{\text{sSFR}} < 10^{-11.2} \text{ yr}^{-1}$  as quiescent.

on the stellar populations, and dust (Bernardi et al. 2017). We also do not account for differences in the IMF and cosmology. In a subsequent work, we will present a detailed comparison of BGS  $M_*$  measurements using different methods. Overall, we find good agreement with previous SMF measurements, especially in the intermediate  $M_*$  range where we precisely infer the pSMF.

In Figure 4, we present the redshift evolution of the pSMF over  $0.01 < z < 0.17$  in redshift bins of width  $\Delta z = 0.04$ . The shaded region represent the jackknife uncertainties for the pSMF. The solid line represents the pSMF above  $M_{\text{lim}}$  while the dashed lines represent the pSMF below the limit. We only include 4 redshift bins, since  $M_{\text{lim}} > 10^{10.5} M_\odot$  for  $z > 0.17$  (Table 2). The pSMFs in Figure 4 do not reveal a significant redshift dependence given their uncertainties. We note that the large uncertainties for the  $0.01 < z < 0.05$  pSMF is driven by large-scale structure at RA  $\sim 195$  deg, Dec  $\sim 28$  deg, and  $z \sim 0.0244$ . The main BGS survey will observe  $> 100\times$  more BGS galaxies than the One-Percent Survey with comparable signal-to-noise,<sup>4</sup> and enable pSMF measurements with unprecedented precision.

#### 4.2. Star-Forming and Quiescent Galaxies in the BGS

In addition to the pSMF of the full galaxy population, we can also examine the pSMF of the star-forming and quiescent subpopulations using  $\overline{\text{SFR}}$ , average SFR over the last 1 Gyr, inferred with PROVABGS. In Figure 5, we present the distribution of  $M_*$  versus average specific SFR,  $\overline{\text{sSFR}} = \overline{\text{SFR}}/M_*$ , for BGS Bright (blue) and Faint (orange) galaxies at  $z < 0.2$ . The  $M_* - \overline{\text{sSFR}}$  distribution of the BGS galaxies reveal a clear bi-modality with star-forming galaxies lying on the SFS and quiescent galaxies lying  $\gtrsim 1$  dex below the sequence. Figure 5 also confirms that BGS Faint galaxies have overall lower  $M_*$  than BGS Bright galaxies and are primarily star-forming galaxies. This is due

<sup>4</sup> The One-Percent Survey was observed using exposure times  $1.2\times$  longer than the main survey.

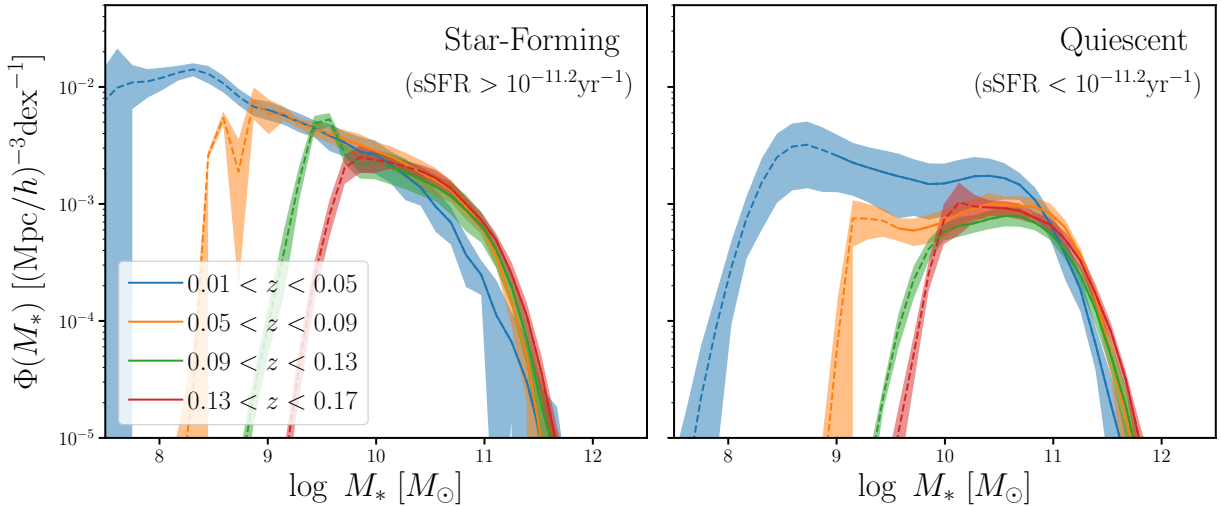


**Figure 6.** The pSMF of star-forming (left) and quiescent (right) BGS Bright galaxies over  $0.01 < z < 0.17$  in bins of  $\Delta z = 0.04$ . Star-forming and quiescent galaxies are classified using an empirically determined  $\text{sSFR} = 10^{-11.2} \text{yr}^{-1}$  cut. We represent the uncertainties for the pSMF in the shaded regions and the pSMFs above/below the  $M_*$  completeness limits in solid/dashed lines. We find little overall evolution of the pSMFs over the redshift range investigated here.

to the fact that the  $(z - W1) - 1.2(g - r) + 1.2$  color used to select BGS Faint galaxies is a proxy for  $\text{H}\alpha$  and  $\text{H}\beta$  emission lines.

To further examine the star-forming and quiescent galaxy populations, we classify BGS Bright galaxies as star-forming or quiescent using a  $\overline{\text{sSFR}} = 10^{-11.2} \text{yr}^{-1}$  cut. We determine this cut empirically based roughly on the  $\overline{\text{sSFR}}$  of the “green valley” between the SFS and the quiescent mode. We opt for a  $\overline{\text{sSFR}}$  cut rather than more sophisticated methods in the literature (*e.g.* Hahn et al. 2019; Donnari et al. 2019) for simplicity. In Figure 6, we present the pSMF of star-forming and quiescent BGS Bright galaxies at  $0.01 < z < 0.17$  in bins of  $\Delta z = 0.04$ . The shaded regions represent the jackknife uncertainties for the pSMF. The solid lines represent the pSMFs above the completeness limit while the dashed lines represent the pSMFs below the limit. Overall, the pSMFs show little evolution over these  $M_*$  and redshift ranges except for a possible decline at the massive end of the star-forming pSMF.

Next, we present the fraction of quiescent galaxies in BGS Bright as a function of  $M_*$  over  $0.01 < z < 0.17$  in Figure 7. The quiescent fraction is derived by taking the ratio of the pSMFs of quiescent galaxies over all galaxies and measured for each  $\Delta z = 0.04$  bin. The shaded region represent the uncertainties derived from propagating the jackknife uncertainties of the pSMFs. We focus on the quiescent fraction of BGS Bright galaxies above the  $M_*$  completeness limit:  $M_* > M_{\text{lim}}$ . At each redshift bin, the quiescent fraction increases with  $M_*$  to  $\sim 1$  at  $M_* \sim 10^{11.5} M_\odot$ . We find no significant redshift evolution of quiescent fraction across  $0.01 < z < 0.17$ . Although the significant statistical uncertainties obfuscate a clear trend, the quiescent fraction evolution is in good qualitative agreement with previous works (*e.g.* Baldry et al. 2006; Iovino et al. 2010; Peng et al. 2010; Hahn et al. 2015).

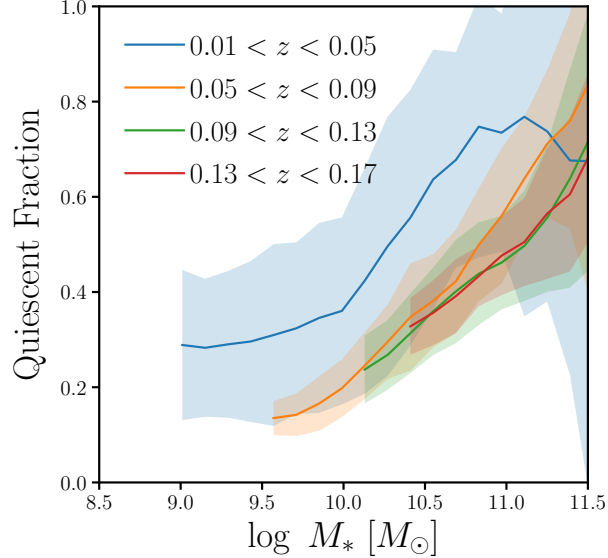


**Figure 7.** The quiescent fraction of BGS Bright galaxies over  $0.01 < z < 0.17$  in bins of  $\Delta z = 0.04$ . We present the uncertainties in the shaded region and only include the quiescent fraction above the  $M_*$  completeness limit. The quiescent fractions increase with  $M_*$  at all redshifts. Furthermore, the quiescent fractions suggest an overall increase in the quiescent population with lower redshift. We find no significant redshift evolution of the quiescent fraction over our redshift range.

Upcoming observations from the DESI main survey will increase the number of BGS galaxies by  $>100\times$  and enable precise comparisons of the quiescent fraction measurements.

## 5. SUMMARY AND DISCUSSION

Over its five-year operation, starting on May 2021, the DESI Bright Galaxy Survey (BGS) will observe the spectra of  $\sim 15$  million galaxies out to  $z < 0.6$  over  $14,000 \text{ deg}^2$ . BGS will produce two main galaxy samples: a  $r < 19.5$  magnitude-limited BGS Bright sample and a fainter  $19.5 < r < 20.175$  surface brightness and color selected BGS Faint sample. Compared to the SDSS main galaxy survey, the BGS galaxy samples will be over two magnitudes deeper, twice the sky, and double the median redshift  $z \sim 0.2$ . They will include diverse galaxy subpopulations that have the potential to reveal new trends among galaxies that were previously undetectable and open new discovery space.

In addition, each galaxy in BGS will have measurements of its detailed physical properties (*e.g.*  $M_*$ , SFR,  $Z_*$ ,  $t_{\text{age}}$ ) from PROVABGS. These properties will be inferred from DESI spectrophotometry using state-of-the-art SED modeling in a fully Bayesian inference framework. PROVABGS will provide statistically rigorous estimates of uncertainties and degeneracies among the properties. With these measurements alongside its statistical power, BGS will provide a powerful galaxy sample with which to measure scaling relations and population statistics that will characterize the global galaxy population and test galaxy formation models with unprecedented precision.

In this work, we showcase the potential of BGS by presenting the probabilistic stellar mass function (pSMF) using  $\sim 250,000$  BGS galaxies observed solely during one of DESI’s survey validation program. The pSMF are derived using a hierarchical population inference framework that statistically and

rigorously propagates uncertainties on  $M_*$  and provide improved estimates of the SMF at the lowest and highest  $M_*$  regimes. We also describe how we account for selection effects and incompleteness in the BGS observations (Appendix A). Overall, we find good agreement between our pSMF and previous SMF measurements in the literature. We also examine the pSMF of the star-forming and quiescent galaxy population classified using a simple  $\overline{\text{sSFR}} = 10^{-11.2} \text{yr}^{-1}$  cut and find qualitative agreement with previous works.

This work is first of a series of papers that will present population statistics for BGS galaxies using PROVABGS. For the pSMF in this work, we used a flexible GMM to provide a non-parametric measurement of the SMF. In a subsequent work, Speranza *et al.* (in prep.), we will present the pSMF of BGS measured using a parametric model with continuous redshift evolution. In another work, we will present in depth comparison of  $M_*$  measured using different methodologies and assumptions. We will also explore the color dependence of the fiber aperture effect and its impact on inferred galaxy properties in Ramos *et al.* (in prep.). Lastly, the hierarchical population inference framework presented in this work can be extended to population statistics beyond the SMF. We will extend the framework to the SFR- $M_*$  distribution and present the probabilistic SFR- $M_*$  distribution and quiescent fraction in future work.

All of the pSMFs presented in this work are measured from BGS galaxies observed from April to May of 2021 during the DESI One-Percent Survey. Since then, DESI has already completed nearly two years of observations. As of writing (May 2023), DESI has observed over 22 million galaxy spectra in total and over 10 million BGS galaxy spectra. With three out of the five years of operation remaining, BGS has completed completed  $\sim 60\%$  of its observations and is ahead of schedule. BGS will also be further extended by additional low-redshift dwarf galaxies observed with the DESI low- $z$  secondary program (Darragh-Ford *et al.* 2022). DESI observations will be publicly released periodically, starting with the Early Data Release (EDR) later this year. The EDR will include observations from the One-Percent Survey used in this work. An accompanying PROVABGS catalog will be released with each data release. All of the pSMF measurements and data used to generate the figures presented in this work is publicly available at <https://doi.org/10.5281/zenodo.8018936>.

## ACKNOWLEDGEMENTS

It's a pleasure to thank Alex I. Malz and Peter Melchior for helpful discussions. We also thank Rita Tojeiro and Rebecca Canning for their detailed review and feedback on an earlier version of this work. This work was supported by the AI Accelerator program of the Schmidt Futures Foundation.

This material is based upon work supported by the U.S. Department of Energy (DOE), Office of Science, Office of High-Energy Physics, under Contract No. DE-AC02-05CH11231, and by the National Energy Research Scientific Computing Center, a DOE Office of Science User Facility under the same contract. Additional support for DESI was provided by the U.S. National Science Foundation (NSF), Division of Astronomical Sciences under Contract No. AST-0950945 to the NSF's National Optical-Infrared Astronomy Research Laboratory; the Science and Technologies Facilities Council of the United Kingdom; the Gordon and Betty Moore Foundation; the Heising-Simons Foundation; the French Alternative Energies and Atomic Energy Commission (CEA); the National Council of Science

and Technology of Mexico (CONACYT); the Ministry of Science and Innovation of Spain (MICINN), and by the DESI Member Institutions: <https://www.desi.lbl.gov/collaborating-institutions>.

The DESI Legacy Imaging Surveys consist of three individual and complementary projects: the Dark Energy Camera Legacy Survey (DECaLS), the Beijing-Arizona Sky Survey (BASS), and the Mayall z-band Legacy Survey (MzLS). DECaLS, BASS and MzLS together include data obtained, respectively, at the Blanco telescope, Cerro Tololo Inter-American Observatory, NSF’s NOIRLab; the Bok telescope, Steward Observatory, University of Arizona; and the Mayall telescope, Kitt Peak National Observatory, NOIRLab. NOIRLab is operated by the Association of Universities for Research in Astronomy (AURA) under a cooperative agreement with the National Science Foundation. Pipeline processing and analyses of the data were supported by NOIRLab and the Lawrence Berkeley National Laboratory. Legacy Surveys also uses data products from the Near-Earth Object Wide-field Infrared Survey Explorer (NEOWISE), a project of the Jet Propulsion Laboratory/California Institute of Technology, funded by the National Aeronautics and Space Administration. Legacy Surveys was supported by: the Director, Office of Science, Office of High Energy Physics of the U.S. Department of Energy; the National Energy Research Scientific Computing Center, a DOE Office of Science User Facility; the U.S. National Science Foundation, Division of Astronomical Sciences; the National Astronomical Observatories of China, the Chinese Academy of Sciences and the Chinese National Natural Science Foundation. LBNL is managed by the Regents of the University of California under contract to the U.S. Department of Energy. The complete acknowledgments can be found at <https://www.legacysurvey.org/>.

Any opinions, findings, and conclusions or recommendations expressed in this material are those of the author(s) and do not necessarily reflect the views of the U. S. National Science Foundation, the U. S. Department of Energy, or any of the listed funding agencies.

The authors are honored to be permitted to conduct scientific research on Iolkam Du’ag (Kitt Peak), a mountain with particular significance to the Tohono O’odham Nation.

## APPENDIX

### A. SPECTROSCOPIC COMPLETENESS

Spectroscopic galaxy surveys, such as BGS, do not successfully measure the redshift for all of the galaxies they target. As a result, this spectroscopic incompleteness must be accounted for when measuring galaxy population statistics such as the SMF. In this appendix, we present how we estimate the spectroscopic incompleteness for BGS and derive the weights we use to correct for its impact on the SMF.

For BGS, spectroscopic incompleteness is primarily driven by fiber assignment and redshift failures. DESI uses 10 fiber-fed spectrographs with 5000 fibers but targets more galaxies than available fibers. For instance, the BGS Bright and Faint samples have  $\sim 860$  and  $530$  targets/deg<sup>2</sup>, respectively. In addition, of the 5000, a minimum of 400 ‘sky’ fibers are dedicated to measuring the sky background for accurate sky subtraction and an additional 100 fibers are assigned to standard stars for flux calibration [Guy et al. \(2023\)](#).

Furthermore, each fiber is controlled by a robotic fiber positioner on the focal plane. These positioners can rotate on two arms and be positioned within a circular patrol region of radius 1.48 arcmin (Schubnell et al. 2016; DESI Collaboration et al. 2016a; Abareshi et al. 2022; Silber et al. 2023). Although the patrol regions of adjacent positioners slightly overlap, the geometry of the positioners cause higher incompleteness in regions with high target density (Smith et al. 2019). To mitigate the incompleteness from the fiber assignment, BGS will observe its footprint with four passes. With this strategy, BGS achieves  $\sim 80\%$  fiber assignment completeness (Hahn et al. 2022b).

To estimate fiber assignment completeness, we run the fiber assignment algorithm (Raichoor et al. 2023) on BGS targets 128 separate times. For each BGS galaxy,  $i$ , we count the total number of times out of 128 fiber assigned realizations that the galaxy is assigned a fiber:  $N_{i,FA}$ . Then to correct for the fiber assignment incompleteness, we assign correction weights

$$w_{i,FA} = \frac{128}{N_{i,FA}} \quad (\text{A1})$$

to each BGS galaxy.

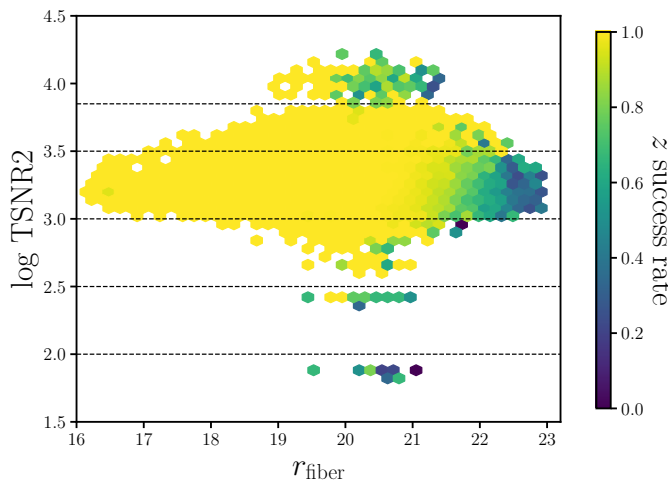


**Figure 8.** Redshift success rate of BGS Bright galaxies as a function of  $r_{\text{fiber}}$  and TSNR2. TSNR2 is a statistic that quantifies the signal-to-noise ratio of the observed spectrum. The color map represents the mean redshift success rate in each hexbin. We mark the TSNR2 bins (black dashed) that we use to separately fit the redshift success rate as a function of  $r_{\text{fiber}}$  using Eq. A3. In each TSNR2 bin, redshift success decreases as  $r_{\text{fiber}}$  increases.

Although we measure a spectrum for each galaxy assigned a fiber, we do not measure reliable redshifts for every spectra that meet the criteria specified in Section 2. This redshift measurement failure significantly contributes to spectroscopic incompleteness. For BGS, redshift failure of an observed galaxy spectrum depends mainly on fiber magnitude and a statistic, TSNR2. Fiber magnitude is the predicted flux of the BGS object within a  $1.5''$  diameter fiber; we use  $r$ -band fiber magnitude,  $r_{\text{fiber}}$ . TSNR2 roughly corresponds to the signal-to-noise ratio of the spectrum and is the statistic used to calibrate the effective exposure times in DESI observations (Guy et al. 2023).

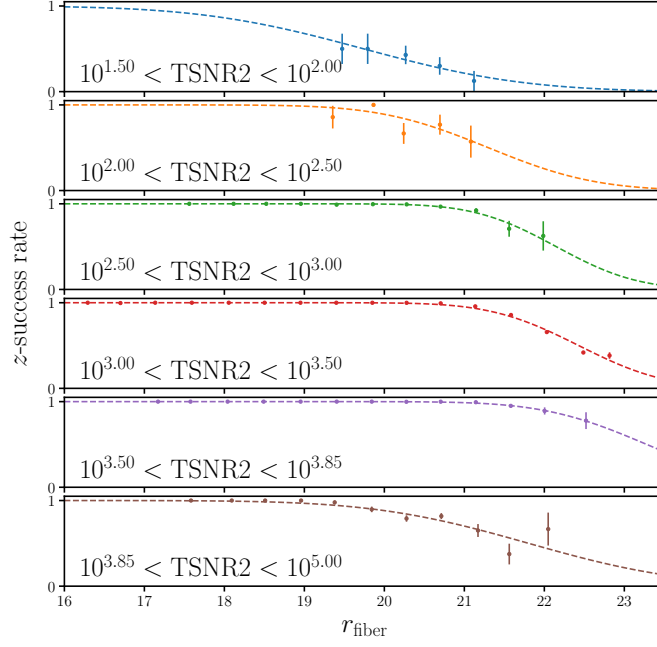


**Figure 9.** Redshift success rates of BGS Bright galaxies as a function of  $r_{\text{fiber}}$  in 6 TSNR2 bins. The error bars represent the Poisson uncertainties. In each panel, we include the best-fit analytic (Eq. A3) approximation of the redshift success rate (dashed) derived from  $\chi^2$  minimization. We use this analytic approximation to calculate the galaxy weights to correct for spectroscopic incompleteness caused by failures to accurately measure redshifts from observed spectra.

In Figure 8, we present the redshift success rate of BGS Bright galaxies as a function of  $r_{\text{fiber}}$  and TSNR2. In each hexbin, the color map represents the mean  $z$ -success rate. We include all hexbins with more than 2 galaxies. Overall, the  $z$ -success rate depends significantly on  $r_{\text{fiber}}$ : galaxies with fainter  $r_{\text{fiber}}$  have lower  $z$ -success rates. However, the  $r_{\text{fiber}}$  dependence itself varies in bins of TSNR2. We mark the edges of the bins in black dashed:  $\log \text{TSNR2} = 2.0, 2.5, 3.0, 3.5, 3.85$ . Within each of the TSNR2 bins, the  $r_{\text{fiber}}$  dependence of the  $z$ -success rate does not vary significantly. In Figure 9, we present the  $z$ -success rate of BGS Bright galaxies as a function of  $r_{\text{fiber}}$  for each of the 6 TSNR2 bins. We mark the range of TSNR2 in the bottom left of each panel. The error bars represent the Poisson uncertainties of the  $z$ -success rate.

To correct for the effect of redshift failures, we include an additional correction weight for each BGS galaxy:

$$w_{i,\text{ZF}} = \frac{1}{f_{z\text{-success}}(r_{\text{fiber},i}, \text{TSNR2}_i)}. \quad (\text{A2})$$

$f_{z\text{-success}}(r_{\text{fiber},i}, \text{TSNR2}_i)$  is the  $z$ -success rate as a function of  $r_{\text{fiber}}$  and TSNR2 of the galaxy. Galaxies with  $f_{z\text{-success}} = 1$  (100%  $z$ -success) will have  $w_{i,\text{ZF}} = 1.0$  while galaxies with  $f_{z\text{-success}} = 0.1$  (10%  $z$ -success) will have  $w_{i,\text{ZF}} = 10$ . For  $f_{z\text{-success}}(r_{\text{fiber},i}, \text{TSNR2}_i)$ , we fit the following functional form for each TSNR2 bin:

$$f_{z\text{-success}}(r_{\text{fiber}}) = \frac{1}{2} \left( 1 - \text{erf}(c_0(r_{\text{fiber}} - c_1)) \right). \quad (\text{A3})$$

**Table 1.** Best-fit coefficients of Eq. A3, which describes the  $z$ -success rate as a function of  $r_{\text{fiber}}$  for different TSNR2 bins for BGS Bright and Faint samples.

TSNR2 range	$c_0$	$c_1$
BGS Bright		
$10^{1.5} - 10^2$	0.443	19.7
$10^2 - 10^{2.5}$	0.668	21.3
$10^{2.5} - 10^3$	0.888	22.1
$10^3 - 10^{3.5}$	0.822	22.4
$10^{3.5} - 10^{3.85}$	0.698	23.3
$10^{3.85} - 10^5$	0.465	21.8
BGS Faint		
$(z - W1) - 1.2(g - r) + 1.2 \geq 0$		
$10^{1.5} - 10^{2.5}$	1.67	21.1
$10^{2.5} - 10^3$	1.65	21.8
$10^3 - 10^{3.1}$	1.49	22.1
$10^{3.1} - 10^{3.2}$	1.32	22.3
$10^{3.2} - 10^{3.3}$	1.33	22.4
$10^{3.3} - 10^{3.5}$	0.907	23.1
$10^{3.5} - 10^{3.85}$	1.03	23.0
$10^{3.85} - 10^5$	0.924	21.6
BGS Faint		
$(z - W1) - 1.2(g - r) + 1.2 < 0$		
$10^{2.5} - 10^3$	1.48	20.9
$10^3 - 10^{3.1}$	2.40	21.2
$10^{3.1} - 10^{3.2}$	1.30	21.8
$10^{3.2} - 10^{3.3}$	1.27	22.0
$10^{3.3} - 10^{3.5}$	1.83	21.6
$10^{3.5} - 10^{3.85}$	0.798	22.9
$10^{3.85} - 10^5$	1.29	20.6

In Figure 9, we present the best-fit  $f_{z\text{-success}}(r_{\text{fiber}})$  for each of the TSNR2 bins in dashed. The best-fit coefficients,  $c_0, c_1$ , are derived from  $\chi^2$  minimization. We repeat this procedure independently for BGS Bright galaxies as well as the BGS Faint galaxies with  $(z - W1) - 1.2(g - r) + 1.2 \geq 0$ , and BGS Faint galaxies with  $(z - W1) - 1.2(g - r) + 1.2 < 0$ . We list the best-fit values in bins of TSNR2 for each of the samples in Table 1.

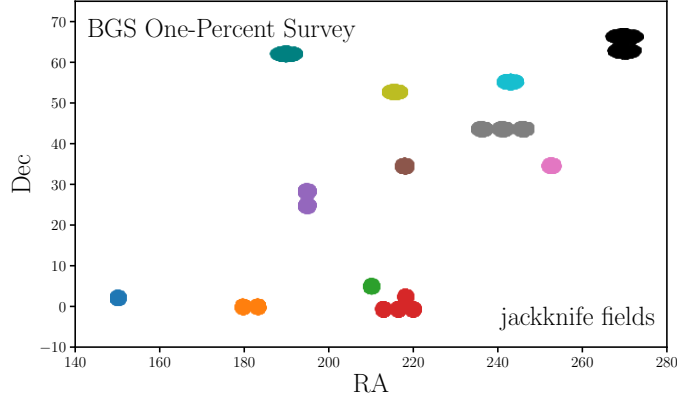


**Figure 10.** The RA and Dec of the 12 jackknife fields of the BGS One-Percent Survey used to estimate the uncertainties on the SMF from sample variance. We mark each field with a distinct color.

## B. UNCERTAINTIES ON THE SMF

We estimate the uncertainties of the pSMF from sample variance using the standard jackknife technique. We split the BGS sample into subsamples and then estimate uncertainties using the subsample-to-subsample variations:

$$\sigma_{\Phi} = \left( \frac{N_{\text{jack}} - 1}{N_{\text{jack}}} \sum_{k=1}^{N_{\text{jack}}} (\Phi_k - \Phi)^2 \right). \quad (\text{B4})$$

$N_{\text{jack}}$  is the number of jackknife subsamples and  $\Phi_k$  represents the SMF estimated from the BGS galaxies excluding the jackknife subsample  $k$ . In this work, we split the BGS sample into 12 jackknife fields based on the angular positions of galaxies. We present the jackknife fields in Figure 10 with distinct colors.

## C. STELLAR MASS COMPLETENESS

In this appendix, we describe how we derive  $M_{\text{lim}}$ , the  $M_*$  limit above which our BGS Bright sample is complete. Although there are various methods for estimating  $M_{\text{lim}}$  in the literature, *e.g.* based on estimating the mass-to-light ratio (Pozzetti et al. 2010; Moustakas et al. 2013), we adopt a simple approach that takes advantage of the fact that BGS Bright is a magnitude-limited sample.

To derive  $M_{\text{lim}}$  in redshift bins of width  $\Delta z = 0.04$ , we first split the galaxy sample into narrower bins of  $\Delta z/2$ . For each narrower redshift bin,  $i\Delta z/2 < z < (i+1)\Delta z/2$ , we take the best-fit PROV-ABGS SEDs for all of the galaxies in the bin and artificially redshift them to  $z' = z + \Delta z/2$ . Then at  $z'$ , the galaxies would have fluxes of

$$f'_{\lambda} = f_{\lambda} \frac{d_L(z)^2}{d_L(z')^2}. \quad (\text{C5})$$

$d_L(z)$  represents the luminosity distance at redshift  $z$ . Afterward, we calculate the  $r$ -band magnitudes,  $r'$ , for  $f'_{\lambda}$  and impose the  $r' < 19.5$  magnitude limit of the BGS Bright. We then compare the  $M_*$

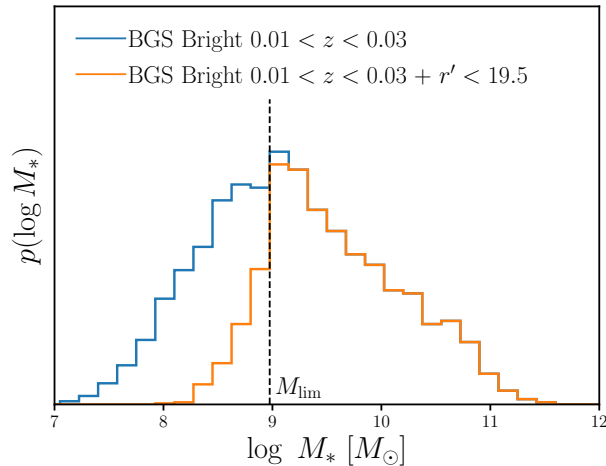


**Figure 11.** The  $M_*$  distribution of BGS Bright galaxies with  $0.01 < z < 0.03$  (blue) and the  $M_*$  distribution of same set of galaxies that would remain in the BGS Bright magnitude limit if they were redshifted to  $z' = z + 0.02$ . We set the stellar mass completeness limit,  $M_{\text{lim}}$ , for  $0.01 < z < 0.05$  to the  $M_*$  where more than 10% of galaxies are excluded in the latter distribution. For each  $\Delta z$  bin, we repeat this procedure to derive  $M_{\text{lim}}$  values.

**Table 2.** Stellar mass completeness limit,  $M_{\text{lim}}$  for redshift bins of width  $\Delta z = 0.04$ .

$z$ range	$\log_{10} M_{\text{lim}}$
0.01 – 0.05	8.975
0.05 – 0.09	9.500
0.09 – 0.13	10.20
0.13 – 0.17	10.38
0.17 – 0.21	10.72

distribution of all the galaxies in  $i\Delta z/2 < z < (i+1)\Delta z/2$  to the galaxies in  $(i+1)\Delta z/2 < z < (i+2)\Delta z/2$  with  $r' < 19.5$ . For instance, we present the  $M_*$  distributions of all BGS Bright galaxies in  $0.01 < z < 0.03$  (blue) and the BGS Bright galaxies in  $0.01 < z < 0.03$  with  $r' < 19.5$  (orange) in Figure 11.

Since galaxies become fainter when they are placed at higher redshifts, *i.e.*  $r' > r$ , the  $r' < 19.5$  sample has fewer low  $M_*$  galaxies. We determine the  $M_*$  at which, more than 10% of galaxies are excluded in the  $r' < 19.5$  sample (black dashed) and set this limit as  $M_{\text{lim}}$  for the redshift bins:  $0.01 < z < 0.05$ . Our procedure for deriving  $M_{\text{lim}}$  takes advantage of the fact that galaxy samples at lower redshifts are complete down to lower  $M_*$  than at higher redshifts. We repeat this procedure for all the  $\Delta z = 0.04$  redshift bins that we use to measure the SMF. In Table 2, we list  $M_{\text{lim}}$  values for each of the redshift bins. Furthermore, we present the  $M_*$  and redshift relation of BGS Bright galaxies (black) and the stellar mass complete sample (blue) in Figure 12.

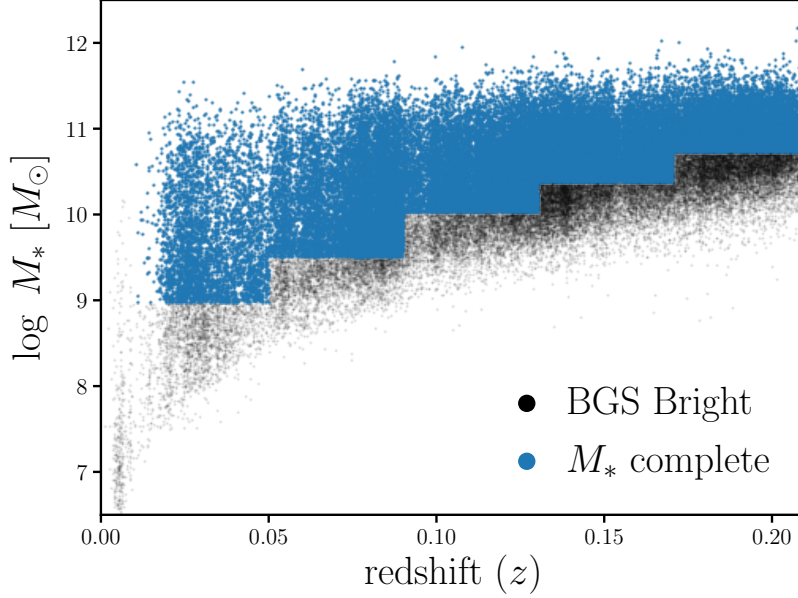


**Figure 12.**  $M_*$  and redshift relation of BGS Bright galaxies in the One-Percent Survey (black) and the galaxies within the stellar mass completeness limit ( $M_* < M_{\text{lim}}$ ; blue).  $M_{\text{lim}}$  is derived in redshift bins of width  $\Delta z = 0.04$ . The lowest redshift bin ( $0.01 < z < 0.05$ ) is complete down to  $M_* < 10^9 M_\odot$ .

#### D. AUTHOR AFFILIATIONS

<sup>1</sup>Department of Astrophysical Sciences, Princeton University, Peyton Hall, Princeton NJ 08544, USA

<sup>2</sup>Lawrence Berkeley National Laboratory, 1 Cyclotron Road, Berkeley, CA 94720, USA

<sup>3</sup>Tata Institute of Fundamental Research, Homi Bhabha Road, Mumbai 400005, India

<sup>4</sup>Physics Dept., Boston University, 590 Commonwealth Avenue, Boston, MA 02215, USA <sup>5</sup>Department of Physics & Astronomy, University College London, Gower Street, London, WC1E 6BT, UK

<sup>6</sup>Institute for Computational Cosmology, Department of Physics, Durham University, South Road, Durham DH1 3LE, UK

<sup>7</sup>Instituto de Física, Universidad Nacional Autónoma de México, Cd. de México C.P. 04510, México

<sup>8</sup>Institut de Física d'Altes Energies (IFAE), The Barcelona Institute of Science and Technology, Campus UAB, 08193 Bellaterra Barcelona, Spain

<sup>9</sup>Departamento de Física, Universidad de los Andes, Cra. 1 No. 18A-10, Edificio Ip, CP 111711, Bogotá, Colombia

<sup>10</sup>Observatorio Astronómico, Universidad de los Andes, Cra. 1 No. 18A-10, Edificio H, CP 111711 Bogotá, Colombia

<sup>11</sup>Center for Cosmology and AstroParticle Physics, The Ohio State University, 191 West Woodruff Avenue, Columbus, OH 43210, USA

<sup>12</sup>Department of Physics, The Ohio State University, 191 West Woodruff Avenue, Columbus, OH 43210, USA

<sup>13</sup>Department of Astronomy, Tsinghua University, 30 Shuangqing Road, Haidian District, Beijing, China, 100190

<sup>14</sup>NSF's NOIRLab, 950 N. Cherry Ave., Tucson, AZ 85719, USA

<sup>15</sup>Institució Catalana de Recerca i Estudis Avançats, Passeig de Lluís Companys, 23, 08010 Barcelona, Spain

<sup>16</sup>Department of Physics and Astronomy, Siena College, 515 Loudon Road, Loudonville, NY 12211, USA

<sup>17</sup>National Astronomical Observatories, Chinese Academy of Sciences, A20 Datun Rd., Chaoyang District, Beijing, 100012, P.R. China

<sup>18</sup>Space Sciences Laboratory, University of California, Berkeley, 7 Gauss Way, Berkeley, CA 94720, USA

<sup>19</sup>University of California, Berkeley, 110 Sproul Hall #5800 Berkeley, CA 94720, USA

<sup>20</sup>Department of Physics and Astronomy, Sejong University, Seoul, 143-747, Korea

<sup>21</sup>CIEMAT, Avenida Complutense 40, E-28040 Madrid, Spain

<sup>22</sup>Korea Astronomy and Space Science Institute, 776, Daedeokdae-ro, Yuseong-gu, Daejeon 34055, Republic of Korea

<sup>23</sup>Department of Physics, University of Michigan, Ann Arbor, MI 48109, USA

<sup>24</sup>University of Michigan, Ann Arbor, MI 48109, USA

<sup>25</sup>Department of Physics & Astronomy, Ohio University, Athens, OH 45701, USA

<sup>26</sup>Institute of Space Sciences, ICE-CSIC, Campus UAB, Carrer de Can Magrans s/n, 08913 Bellaterra, Barcelona, Spain

<sup>27</sup>Kavli Institute for Particle Astrophysics and Cosmology, Stanford University, Menlo Park, CA 94305, USA

<sup>28</sup>Physics Department, Stanford University, Stanford, CA 93405, USA

<sup>29</sup>SLAC National Accelerator Laboratory, Menlo Park, CA 94305, USA

## REFERENCES

- Abareshi, B., Aguilar, J., Ahlen, S., et al. 2022, Overview of the Instrumentation for the Dark Energy Spectroscopic Instrument, doi: [10.48550/arXiv.2205.10939](https://doi.org/10.48550/arXiv.2205.10939)
- Alexander, D. M., Davis, T. M., Chaussidon, E., et al. 2023, *AJ*, 165, 124, doi: [10.3847/1538-3881/acacfc](https://doi.org/10.3847/1538-3881/acacfc)
- Allende Prieto, C., Cooper, A. P., Dey, A., et al. 2020, *Research Notes of the American Astronomical Society*, 4, 188, doi: [10.3847/2515-5172/abc1dc](https://doi.org/10.3847/2515-5172/abc1dc)
- Bailey et al. 2023
- Baldry, I. K., Balogh, M. L., Bower, R. G., et al. 2006, *Monthly Notices of the Royal Astronomical Society*, 373, 469, doi: [10.1111/j.1365-2966.2006.11081.x](https://doi.org/10.1111/j.1365-2966.2006.11081.x)
- Baronchelli, L., Nandra, K., & Buchner, J. 2020, *Monthly Notices of the Royal Astronomical Society*, 498, 5284, doi: [10.1093/mnras/staa2684](https://doi.org/10.1093/mnras/staa2684)
- Behroozi, P., Wechsler, R. H., Hearin, A. P., & Conroy, C. 2019, *Monthly Notices of the Royal Astronomical Society*, 1134, doi: [10.1093/mnras/stz1182](https://doi.org/10.1093/mnras/stz1182)
- Benson, A. J. 2012, *New Astronomy*, 17, 175, doi: [10.1016/j.newast.2011.07.004](https://doi.org/10.1016/j.newast.2011.07.004)
- Bernardi, M., Meert, A., Sheth, R. K., et al. 2017, *Monthly Notices of the Royal Astronomical Society*, 467, 2217, doi: [10.1093/mnras/stx176](https://doi.org/10.1093/mnras/stx176)
- Blanton, M. R., & Moustakas, J. 2009, *Annual Review of Astronomy and Astrophysics*, 47, 159, doi: [10.1146/annurev-astro-082708-101734](https://doi.org/10.1146/annurev-astro-082708-101734)
- Blanton, M. R., Hogg, D. W., Bahcall, N. A., et al. 2003, *ApJ*, 592, 819, doi: [10.1086/375776](https://doi.org/10.1086/375776)

- Bolton, A. S., & Schlegel, D. J. 2010, *PASP*, 122, 248, doi: [10.1086/651008](https://doi.org/10.1086/651008)
- Brodzeller et al. 2023
- Chabrier, G. 2003, *Publications of the Astronomical Society of the Pacific*, 115, 763, doi: [10.1086/376392](https://doi.org/10.1086/376392)
- Charlot, S., & Fall, S. M. 2000, *ApJ*, 539, 718, doi: [10.1086/309250](https://doi.org/10.1086/309250)
- Chaussidon, E., Yèche, C., Palanque-Delabrouille, N., et al. 2023, *ApJ*, 944, 107, doi: [10.3847/1538-4357/acb3c2](https://doi.org/10.3847/1538-4357/acb3c2)
- Choi, J., Dotter, A., Conroy, C., et al. 2016, *The Astrophysical Journal*, 823, 102, doi: [10.3847/0004-637X/823/2/102](https://doi.org/10.3847/0004-637X/823/2/102)
- Coil, A. L., Blanton, M. R., Burles, S. M., et al. 2011, *The Astrophysical Journal*, 741, 8, doi: [10.1088/0004-637X/741/1/8](https://doi.org/10.1088/0004-637X/741/1/8)
- Conroy, C., Gunn, J. E., & White, M. 2009, *The Astrophysical Journal*, 699, 486, doi: [10.1088/0004-637X/699/1/486](https://doi.org/10.1088/0004-637X/699/1/486)
- Conroy, C., White, M., & Gunn, J. E. 2010, *The Astrophysical Journal*, 708, 58, doi: [10.1088/0004-637X/708/1/58](https://doi.org/10.1088/0004-637X/708/1/58)
- Cooper, A. P., Kopusov, S. E., Allende Prieto, C., et al. 2022, arXiv e-prints, arXiv:2208.08514. <https://arxiv.org/abs/2208.08514>
- Daddi, E., Dickinson, M., Morrison, G., et al. 2007, *The Astrophysical Journal*, 670, 156, doi: [10.1086/521818](https://doi.org/10.1086/521818)
- Darragh-Ford, E., Wu, J. F., Mao, Y.-Y., et al. 2022, arXiv e-prints, arXiv:2212.07433, doi: [10.48550/arXiv.2212.07433](https://doi.org/10.48550/arXiv.2212.07433)
- Davé, R., Rafieferantsoa, M. H., & Thompson, R. J. 2017, arXiv:1704.01135 [astro-ph]. <http://ascl.net/1704.01135>
- DESI Collaboration, Aghamousa, A., Aguilar, J., et al. 2016a, arXiv:1611.00036 [astro-ph]. <http://ascl.net/1611.00036>
- . 2016b, arXiv:1611.00037 [astro-ph]. <http://ascl.net/1611.00037>
- DESI Collaboration, Adame, A. G., Aguilar, J., et al. 2023a, arXiv e-prints, arXiv:2306.06307, doi: [10.48550/arXiv.2306.06307](https://doi.org/10.48550/arXiv.2306.06307)
- . 2023b, arXiv e-prints, arXiv:2306.06308, doi: [10.48550/arXiv.2306.06308](https://doi.org/10.48550/arXiv.2306.06308)
- Dey, A., Schlegel, D. J., Lang, D., et al. 2019, *AJ*, 157, 168, doi: [10.3847/1538-3881/ab089d](https://doi.org/10.3847/1538-3881/ab089d)
- Dickey, C. M., Starkenburg, T. K., Geha, M., et al. 2021, *The Astrophysical Journal*, 915, 53, doi: [10.3847/1538-4357/abc014](https://doi.org/10.3847/1538-4357/abc014)
- Donnari, M., Pillepich, A., Nelson, D., et al. 2021, *Monthly Notices of the Royal Astronomical Society*, 506, 4760, doi: [10.1093/mnras/stab1950](https://doi.org/10.1093/mnras/stab1950)
- . 2019, *Monthly Notices of the Royal Astronomical Society*, 485, 4817, doi: [10.1093/mnras/stz712](https://doi.org/10.1093/mnras/stz712)
- Dotter, A. 2016, *The Astrophysical Journal Supplement Series*, 222, 8, doi: [10.3847/0067-0049/222/1/8](https://doi.org/10.3847/0067-0049/222/1/8)
- Driver, S. P., Hill, D. T., Kelvin, L. S., et al. 2011, *Monthly Notices of the Royal Astronomical Society*, 413, 971, doi: [10.1111/j.1365-2966.2010.18188.x](https://doi.org/10.1111/j.1365-2966.2010.18188.x)
- Driver, S. P., Bellstedt, S., Robotham, A. S. G., et al. 2022, *Monthly Notices of the Royal Astronomical Society*, stac472, doi: [10.1093/mnras/stac472](https://doi.org/10.1093/mnras/stac472)
- Foreman-Mackey, D., Hogg, D. W., & Morton, T. D. 2014, *The Astrophysical Journal*, 795, 64, doi: [10.1088/0004-637X/795/1/64](https://doi.org/10.1088/0004-637X/795/1/64)
- Franx, M., van Dokkum, P. G., Förster Schreiber, N. M., et al. 2008, *ApJ*, 688, 770, doi: [10.1086/592431](https://doi.org/10.1086/592431)
- Genel, S., Vogelsberger, M., Springel, V., et al. 2014, *Monthly Notices of the Royal Astronomical Society*, 445, 175, doi: [10.1093/mnras/stu1654](https://doi.org/10.1093/mnras/stu1654)
- Guy, J., Bailey, S., Kremin, A., et al. 2023, *AJ*, 165, 144, doi: [10.3847/1538-3881/acb212](https://doi.org/10.3847/1538-3881/acb212)
- Hahn, C., Tinker, J. L., & Wetzel, A. R. 2017, *The Astrophysical Journal*, 841, 6, doi: [10.3847/1538-4357/aa6d6b](https://doi.org/10.3847/1538-4357/aa6d6b)
- Hahn, C., Blanton, M. R., Moustakas, J., et al. 2015, *The Astrophysical Journal*, 806, 162, doi: [10.1088/0004-637X/806/2/162](https://doi.org/10.1088/0004-637X/806/2/162)
- Hahn, C., Starkenburg, T. K., Choi, E., et al. 2019, *The Astrophysical Journal*, 872, 160, doi: [10.3847/1538-4357/aafedd](https://doi.org/10.3847/1538-4357/aafedd)
- Hahn, C., Starkenburg, T. K., Anglés-Alcázar, D., et al. 2021, IQ Collaboratory III: The Empirical Dust Attenuation Framework – Taking Hydrodynamical Simulations with a Grain of Dust
- Hahn, C., Kwon, K. J., Tojeiro, R., et al. 2022a, *The DESI PRObabilistic Value-Added Bright Galaxy Survey (PROVABGS) Mock Challenge*
- Hahn, C., Wilson, M. J., Ruiz-Macias, O., et al. 2022b, *DESI Bright Galaxy Survey: Final Target Selection, Design, and Validation*

- Henriques, B. M. B., Thomas, P. A., Oliver, S., & Roseboom, I. 2009, *Monthly Notices of the Royal Astronomical Society*, 396, 535, doi: [10.1111/j.1365-2966.2009.14730.x](https://doi.org/10.1111/j.1365-2966.2009.14730.x)
- Henriques, B. M. B., White, S. D. M., Thomas, P. A., et al. 2015, *Monthly Notices of the Royal Astronomical Society*, 451, 2663, doi: [10.1093/mnras/stv705](https://doi.org/10.1093/mnras/stv705)
- Hogg, D. W., Myers, A. D., & Bovy, J. 2010, *The Astrophysical Journal*, 725, 2166, doi: [10.1088/0004-637X/725/2/2166](https://doi.org/10.1088/0004-637X/725/2/2166)
- Ilbert, O., McCracken, H. J., Le Fèvre, O., et al. 2013, *A&A*, 556, A55, doi: [10.1051/0004-6361/201321100](https://doi.org/10.1051/0004-6361/201321100)
- Iovino, A., Cucciati, O., Scodeggio, M., et al. 2010, *Astronomy and Astrophysics*, 509, A40, doi: [10.1051/0004-6361/200912558](https://doi.org/10.1051/0004-6361/200912558)
- Jamieson, D., Li, Y., Alves de Oliveira, R., et al. 2022, *Field Level Neural Network Emulator for Cosmological N-body Simulations*
- Karamanis, M., & Beutler, F. 2020, arXiv e-prints, arXiv:2002.06212
- Kingma, D. P., & Ba, J. 2017, arXiv:1412.6980 [cs]. <http://ascl.net/1412.6980>
- Kirkby et al. 2023
- Kwon, K. J., Hahn, C., & Alsing, J. 2022, *Neural Stellar Population Synthesis Emulator for the DESI PROVABGS*
- Lan, T.-W., Tojeiro, R., Armengaud, E., et al. 2023, *ApJ*, 943, 68, doi: [10.3847/1538-4357/aca5fa](https://doi.org/10.3847/1538-4357/aca5fa)
- Leja, J., Speagle, J. S., Johnson, B. D., et al. 2019, arXiv, arXiv:1910.04168
- Lejeune, T., Cuisinier, F., & Buser, R. 1997, *A & S*, 125, 229, doi: [10.1051/aas:1997373](https://doi.org/10.1051/aas:1997373)
- , 1998, *Astronomy and Astrophysics Supplement*, v.130, p.65-75, 130, 65, doi: [10.1051/aas:1998405](https://doi.org/10.1051/aas:1998405)
- Levi, M., Bebek, C., Beers, T., et al. 2013, arXiv e-prints, arXiv:1308.0847, <https://arxiv.org/abs/1308.0847>
- Li, C., & White, S. D. M. 2009, *Monthly Notices of the Royal Astronomical Society*, 398, 2177, doi: [10.1111/j.1365-2966.2009.15268.x](https://doi.org/10.1111/j.1365-2966.2009.15268.x)
- Lu, Y., Wechsler, R. H., Somerville, R. S., et al. 2014, *The Astrophysical Journal*, 795, 123, doi: [10.1088/0004-637X/795/2/123](https://doi.org/10.1088/0004-637X/795/2/123)
- Malz, A. I., & Hogg, D. W. 2020, *How to Obtain the Redshift Distribution from Probabilistic Redshift Estimates*
- Mannucci, F., Cresci, G., Maiolino, R., Marconi, A., & Gnerucci, A. 2010, *MNRAS*, 408, 2115, doi: [10.1111/j.1365-2966.2010.17291.x](https://doi.org/10.1111/j.1365-2966.2010.17291.x)
- Marchesini, D., van Dokkum, P. G., Förster Schreiber, N. M., et al. 2009, *The Astrophysical Journal*, 701, 1765, doi: [10.1088/0004-637X/701/2/1765](https://doi.org/10.1088/0004-637X/701/2/1765)
- McLachlan, G., & Peel, D. 2000, *Finite Mixture Models* (Wiley-Interscience)
- Miller, T. N., Doel, P., Gutierrez, G., et al. 2023, arXiv e-prints, arXiv:2306.06310, doi: [10.48550/arXiv.2306.06310](https://doi.org/10.48550/arXiv.2306.06310)
- Moustakas, J., Coil, A. L., Aird, J., et al. 2013, *The Astrophysical Journal*, 767, 50, doi: [10.1088/0004-637X/767/1/50](https://doi.org/10.1088/0004-637X/767/1/50)
- Muzzin, A., Marchesini, D., Stefanon, M., et al. 2013, *ApJ*, 777, 18, doi: [10.1088/0004-637X/777/1/18](https://doi.org/10.1088/0004-637X/777/1/18)
- Myers, A. D., Moustakas, J., Bailey, S., et al. 2023, *AJ*, 165, 50, doi: [10.3847/1538-3881/aca5f9](https://doi.org/10.3847/1538-3881/aca5f9)
- Nelson, D., Pillepich, A., Genel, S., et al. 2015, *Astronomy and Computing*, 13, 12, doi: [10.1016/j.ascom.2015.09.003](https://doi.org/10.1016/j.ascom.2015.09.003)
- Noeske, K. G., Weiner, B. J., Faber, S. M., et al. 2007, *The Astrophysical Journal Letters*, 660, L43, doi: [10.1086/517926](https://doi.org/10.1086/517926)
- Norberg, P., Baugh, C. M., Gaztañaga, E., & Croton, D. J. 2009, *Monthly Notices of the Royal Astronomical Society*, 396, 19, doi: [10.1111/j.1365-2966.2009.14389.x](https://doi.org/10.1111/j.1365-2966.2009.14389.x)
- Pacifici, C., Iyer, K. G., Mobasher, B., et al. 2023, *The Astrophysical Journal*, 944, 141, doi: [10.3847/1538-4357/acacff](https://doi.org/10.3847/1538-4357/acacff)
- Paxton, B., Bildsten, L., Dotter, A., et al. 2011, *The Astrophysical Journal Supplement Series*, 192, 3, doi: [10.1088/0067-0049/192/1/3](https://doi.org/10.1088/0067-0049/192/1/3)
- Paxton, B., Cantiello, M., Arras, P., et al. 2013, *The Astrophysical Journal Supplement Series*, 208, 4, doi: [10.1088/0067-0049/208/1/4](https://doi.org/10.1088/0067-0049/208/1/4)
- Paxton, B., Marchant, P., Schwab, J., et al. 2015, *The Astrophysical Journal Supplement Series*, 220, 15, doi: [10.1088/0067-0049/220/1/15](https://doi.org/10.1088/0067-0049/220/1/15)
- Peng, Y.-j., Lilly, S. J., Kovač, K., et al. 2010, *The Astrophysical Journal*, 721, 193, doi: [10.1088/0004-637X/721/1/193](https://doi.org/10.1088/0004-637X/721/1/193)

- Planck Collaboration, Ade, P. a. R., Aghanim, N., et al. 2014, *Astronomy & Astrophysics*, Volume 571, id.A16, <NUMPAGES>66</NUMPAGES> pp., 571, A16, doi: [10.1051/0004-6361/201321591](https://doi.org/10.1051/0004-6361/201321591)
- Pozzetti, L., Bolzonella, M., Zucca, E., et al. 2010, *A&A*, 523, A13, doi: [10.1051/0004-6361/200913020](https://doi.org/10.1051/0004-6361/200913020)
- Press, W. H., Teukolsky, S. A., Vetterling, W. T., & Flannery, B. P. 1992, *Numerical Recipes in C (2Nd Ed.): The Art of Scientific Computing* (New York, NY, USA: Cambridge University Press)
- Raichoor, A., Eisenstein, D. J., Karim, T., et al. 2020, *Research Notes of the American Astronomical Society*, 4, 180, doi: [10.3847/2515-5172/abc078](https://doi.org/10.3847/2515-5172/abc078)
- Raichoor, A., Moustakas, J., Newman, J. A., et al. 2023, *AJ*, 165, 126, doi: [10.3847/1538-3881/acb213](https://doi.org/10.3847/1538-3881/acb213)
- Raichoor et al. 2023
- Ruiz-Macias, O., Zarrouk, P., Cole, S., et al. 2020, *Research Notes of the American Astronomical Society*, 4, 187, doi: [10.3847/2515-5172/abc25a](https://doi.org/10.3847/2515-5172/abc25a)
- Saintonge, A., & Catinella, B. 2022, *ARA&A*, 60, 319, doi: [10.1146/annurev-astro-021022-043545](https://doi.org/10.1146/annurev-astro-021022-043545)
- Salim, S., Rich, R. M., Charlot, S., et al. 2007, *The Astrophysical Journal Supplement Series*, 173, 267, doi: [10.1086/519218](https://doi.org/10.1086/519218)
- Sánchez-Blázquez, P., Peletier, R. F., Jiménez-Vicente, J., et al. 2006, *Monthly Notices of the Royal Astronomical Society*, 371, 703, doi: [10.1111/j.1365-2966.2006.10699.x](https://doi.org/10.1111/j.1365-2966.2006.10699.x)
- Santini, P., Castellano, M., Fontana, A., et al. 2022, *ApJ*, 940, 135, doi: [10.3847/1538-4357/ac9a48](https://doi.org/10.3847/1538-4357/ac9a48)
- Schlafly, E. F., Kirkby, D., Schlegel, D. J., et al. 2023, arXiv e-prints, arXiv:2306.06309, doi: [10.48550/arXiv.2306.06309](https://doi.org/10.48550/arXiv.2306.06309)
- Schlegel et al. 2023
- Schubnell, M., Ameel, J., Besuner, R. W., et al. 2016, in *Society of Photo-Optical Instrumentation Engineers (SPIE) Conference Series*, Vol. 9908, *Ground-based and Airborne Instrumentation for Astronomy VI*, ed. C. J. Evans, L. Simard, & H. Takami, 990892, doi: [10.1117/12.2233370](https://doi.org/10.1117/12.2233370)
- Silber, J. H., Fagrelus, P., Fanning, K., et al. 2023, *AJ*, 165, 9, doi: [10.3847/1538-3881/ac9ab1](https://doi.org/10.3847/1538-3881/ac9ab1)
- Smith, A., He, J.-h., Cole, S., et al. 2019, *MNRAS*, 484, 1285, doi: [10.1093/mnras/stz059](https://doi.org/10.1093/mnras/stz059)
- Somerville, R. S., & Davé, R. 2015, *Annual Review of Astronomy and Astrophysics*, 53, 51, doi: [10.1146/annurev-astro-082812-140951](https://doi.org/10.1146/annurev-astro-082812-140951)
- Speagle, J. S., Steinhardt, C. L., Capak, P. L., & Silverman, J. D. 2014, *The Astrophysical Journal Supplement Series*, 214, 15, doi: [10.1088/0067-0049/214/2/15](https://doi.org/10.1088/0067-0049/214/2/15)
- Tacconi, L. J., Genzel, R., & Sternberg, A. 2020, *ARA&A*, 58, 157, doi: [10.1146/annurev-astro-082812-141034](https://doi.org/10.1146/annurev-astro-082812-141034)
- Tinker, J. L., Wetzel, A. R., Conroy, C., & Mao, Y.-Y. 2017, *Monthly Notices of the Royal Astronomical Society*, 472, 2504, doi: [10.1093/mnras/stx2066](https://doi.org/10.1093/mnras/stx2066)
- Trayford, J. W., Camps, P., Theuns, T., et al. 2017, *Monthly Notices of the Royal Astronomical Society*, 470, 771, doi: [10.1093/mnras/stx1051](https://doi.org/10.1093/mnras/stx1051)
- Tremonti, C. A., Heckman, T. M., Kauffmann, G., et al. 2004, *ApJ*, 613, 898, doi: [10.1086/423264](https://doi.org/10.1086/423264)
- van der Wel, A., Franx, M., van Dokkum, P. G., et al. 2014, *ApJ*, 788, 28, doi: [10.1088/0004-637X/788/1/28](https://doi.org/10.1088/0004-637X/788/1/28)
- Villaescusa-Navarro, F., Genel, S., Anglés-Alcázar, D., et al. 2022, arXiv:2201.01300 [astro-ph]. <http://ascl.net/2201.01300>
- Vogelsberger, M., Genel, S., Springel, V., et al. 2014, *Monthly Notices of the Royal Astronomical Society*, 444, 1518, doi: [10.1093/mnras/stu1536](https://doi.org/10.1093/mnras/stu1536)
- Westera, P., Lejeune, T., Buser, R., Cuisinier, F., & Bruzual, G. 2002, *Astronomy and Astrophysics*, 381, 524, doi: [10.1051/0004-6361:20011493](https://doi.org/10.1051/0004-6361:20011493)
- Wetzel, A. R., Tinker, J. L., Conroy, C., & van den Bosch, F. C. 2013, *Monthly Notices of the Royal Astronomical Society*, 432, 336, doi: [10.1093/mnras/stt469](https://doi.org/10.1093/mnras/stt469)
- Yèche, C., Palanque-Delabrouille, N., Claveau, C.-A., et al. 2020, *Research Notes of the American Astronomical Society*, 4, 179, doi: [10.3847/2515-5172/abc01a](https://doi.org/10.3847/2515-5172/abc01a)
- York, D. G., Adelman, J., Anderson, Jr., J. E., et al. 2000, *The Astronomical Journal*, 120, 1579, doi: [10.1086/301513](https://doi.org/10.1086/301513)

Zhou, R., Newman, J. A., Dawson, K. S., et al. 2020, Research Notes of the American Astronomical Society, 4, 181, doi: [10.3847/2515-5172/abc0f4](https://doi.org/10.3847/2515-5172/abc0f4)

Zhou, R., Dey, B., Newman, J. A., et al. 2023, AJ, 165, 58, doi: [10.3847/1538-3881/aca5fb](https://doi.org/10.3847/1538-3881/aca5fb)

Zou, H., Zhou, X., Fan, X., et al. 2017, PASP, 129, 064101, doi: [10.1088/1538-3873/aa65ba](https://doi.org/10.1088/1538-3873/aa65ba)